ORNL/SPR-2024/3511
M3LW-24OR0403013

Light Water Reactor Sustainability Program

High-Resolution 3D Simulation of Irradiated Concrete – Considerations on Flux Effects

Yann Le Pape
Shane Henderson
Igor Remec
Steve Zinkle

August 2024

U.S. Department of Energy
Office of Nuclear Energy

ORNL/SPR-2024/3511
M3LW-24OR0403013

High-Resolution 3D Simulation of Irradiated Concrete: Considerations for Flux Effects

Yann Le Pape
Shane Henderson
Steve Zinkle Igor
Remec

August 30, 2024

OAK RIDGE National Laboratory

ORNL IS MANAGED BY UT-BATTELLE LLC FOR THE US DEPARTMENT OF ENERGY

ORNL/SPR-2024/3511
M3LW-24OR0403013

[1] Nuclear Energy and Fuel Cycle Division
[2] University of Tennessee, Knoxville
[3] Second Target Station

HIGH-RESOLUTION 3D SIMULATION OF IRRADIATED CONCRETE: CONSIDERATIONS FOR FLUX EFFECTS

Yann Le Pape[1]
Shane Henderson[1]
Steve Zinkle[2]
Igor Remec[3]

August 30, 2024

Prepared by
OAK RIDGE NATIONAL LABORATORY
Oak Ridge, TN 37831
managed by
UT-BATTELLE LLC
for the
US DEPARTMENT OF ENERGY
under contract DE-AC05-00OR22725

CONTENTS

LIST OF FIGURES

LIST OF TABLES

LIST OF ABBREVIATIONS

CBS	concrete biological shield
CVR	centrum výskomu ŘeŽ
dpa	displacement per atom
EDS	energy-dispersive x-ray spectroscopy
EFPY	effective full-power year
HCP	hardened cement paste
IFE	Institutt for energiteknikk
IMAC	Irradiated Minerals Aggregate and Concrete
JCAMP	Japan Concrete Aging Management Program
LITR	Low Intensity Test Reactor
LWR	light-water reactor
LWRS	Light Water Reactor Sustainability
m-XRF	micro x-ray fluorescence
MOSAIC	Microstructure Oriented Scientific Analysis of Irradiated Concrete
MTR	Materials Testing Reactor
NRC	U.S. Nuclear Regulatory Commission
ORNL	Oak Ridge National Laboratory
PWR	pressurized water reactor
RIVE	radiation-induced volumetric expansion
RPV	reactor pressure vessel
SEM	scanning electron microscopy
XRD	x-ray diffraction

EXECUTIVE SUMMARY

The primary function of the concrete biological shield (CBS) in light-water reactors (LWRs) is to protect equipment and personnel from neutron and gamma radiation escaping the reactor pressure vessel (RPV). Beyond this radioprotection role, the CBS in many pressurized water reactors (PWRs) also provides structural support to both the RPV and the nuclear steam supply system (NSSS). For the safe and viable long-term operation of LWRs, it is crucial to understand and characterize the effects of neutron and gamma radiation on concrete and its constituents, as well as to develop predictive tools to assess the performance of the CBS under both normal operating and accidental conditions.

The main degradation mechanism is the radiation-induced volumetric expansion (RIVE) of aggregate-forming minerals. The concrete in a LWR's biological shield is generally made of natural aggregate that constitutes about 70% of the concrete volume. Neutron irradiation causes the formation of defects (e.g., Frenkel pairs), voids, and the disordering of the crystalline structure of minerals. This phenomenon at its early stage is called *amorphization* or *metamictization*. Such atomistic mechanisms lead to changes in the physical and chemical properties of minerals, including a change of density (expansive mechanism), the evolution of elastic properties toward isotropy, and the acceleration in the dissolution rate of minerals in presence of high-alkaline solutions, such as that of the cement paste porosity. Minerals' RIVE varies with the chemical composition and the ratio of covalent to ionic bonds. Highly covalent minerals such as quartz, which is a framework silicate, exhibit very large RIVE, up to nearly 18%. Other framework silicates, such as feldspars, may reach up to 8% in RIVE. The maximum RIVE decreases with less structured silicates such as pyroxene and olivine. Because silicates are abundant in the United States, their presence in a biological shield's concrete is very likely. Carbonates (i.e., calcite, dolomite) are much less susceptible to RIVE (maximum expansion estimated <0.3%). Metallic oxides, such as hematite and magnetite found in heavy aggregates, are sometimes used in boiling water reactors' CBSs. Their RIVE is on the order of a few percent.

Aggregates used for the construction of LWRs are extracted from quarries that encompass a range of geological formations, including magmatic, metamorphic, and sedimentary rocks. Regardless of the mechanisms involved in rock formation, aggregates are complex assemblages of various, and sometimes altered, minerals. The diversity of minerals within aggregates leads to mismatched RIVE between adjacent phases when they are subjected to neutron irradiation. This discrepancy results in the formation of both grain boundary and transgranular cracks, which deteriorate the mechanical properties of the aggregate. The extent of this deterioration depends on several factors, including the chemical composition of the aggregates (e.g., silica content), the rock formation mechanism, which influences grain size and boundary properties, and the presence of mineral defects.

Neutron-irradiated concrete is affected mainly by aggregate RIVE and cement paste shrinkage, which cause volumetric change and a degradation of mechanical properties, including Young's modulus as well as tensile and compressive strength at fluences $\gtrapprox 10^{19}$ n·cm^{-2} ($E > 0.1$ MeV). Such a fluence and above is predicted to be reached for all PWRs operating in the United States at 80 years of operation.

The need for predictive modeling and simulation tools for irradiated concrete led to the development of the Microstructure Oriented Simulation and Analysis of Irradiated Concrete (MOSAIC) code. MOSAIC is a fast Fourier transform–based software developed by Oak Ridge National Laboratory for the DOE Light Water Reactor Sustainability Program. MOSAIC is crucial for assessing concrete's susceptibility to damage induced by neutron irradiation because it accounts for the chemical composition and microstructural characteristics of its constituents, which affect the impact of irradiation on concrete.

In this report, irradiation simulations of 3D Microstructure Oriented Scientific Analysis of Irradiated Concrete models, representing realistic and well-characterized microstructures, are presented and compared with

post–neutron irradiation data obtained by the Japan Concrete Aging Management Program team and Oak Ridge National Laboratory for a US Nuclear Regulatory Commission–sponsored activity. The main finding of this analysis is that the neutron flux appears to have a significant effect on the radiation-induced volumetric expansion rate, suggesting that current models likely overestimate the irradiation-induced damage in the in-service concrete used in light-water reactors. The origin of this flux effect is attributed to the annealing of irradiation-induced defects. However, the reinterpretation of data from the literature on irradiated rock-forming minerals suggests that thermal annealing is not responsible for this effect. Ionization-enhanced annealing is proposed as a potential hypothesis.

ACKNOWLEDGMENTS

This research was sponsored by the US Department of Energy (DOE) Office of Nuclear Energy's Light Water Reactor Sustainability Program—Materials Research Pathway—under contract DE-AC05-00OR22725 with UT-Battelle LLC/Oak Ridge National Laboratory (ORNL).

The authors would like to express their deepest appreciation for the fruitful discussions and the exchange of information and materials with the Japan Concrete Aging Management Program (JCAMP). The post-irradiation data used to compare with the MOSAIC simulations presented in this report were either obtained from JCAMP or provided by Oak Ridge National Laboratory (ORNL) through materials shared by JCAMP. Additionally, Professor Maruyama's invited presentation at the Light Water Reactor Sustainability Program Spring Meeting 2024 provided invaluable data supporting the hypothesis regarding the effects of fast neutron flux on radiation-induced damage to concrete-forming aggregates.

1. INTRODUCTION

The collision of fast neutrons ($E > 10$ keV) with the concrete constitutive materials of the concrete biological shield (CBS) causes point-defects and atomic cascades. Aggregate-forming minerals are susceptible to irradiation-damage. The physical mechanism of this deterioration is called *amorphization*: The pristine crystalline structure of the minerals is gradually distorted by deformation and rupture of their ionic and covalent bonds. Amorphization results in changes of physical and engineering properties: density (Primak 1958, 1976; Wong 1974; Denisov, Dubrovskii, and Solovyov 2012; Krivokoneva and Sidorenko 1971; Krivokoneva 1976), elastic properties (Mayer and Lecomte 1960; Krishnan et al. 2018), and dissolution susceptibility in the presence of high-pH solutions (Pignatelli et al. 2016; Hsiao et al. 2017; Hsiao et al. 2018; Hsiao et al. 2019). The main effect is called radiation-induced volumetric expansion (RIVE). Most minerals exhibit a gradual swelling with increasing fluence, generally in the form of sigmoidal curves (Bykov et al. 1981; Denisov, Dubrovskii, and Solovyov 2012; Le Pape, Alsaid, and Giorla 2018). However, there are exceptions to that rule: vitreous forms of quartz (e.g., chert, opal) exhibit shrinkage (Mayer and Lecomte 1960; Primak and Kampwirth 1968). The amplitude of RIVE varies greatly with the mineralogy, from $< 1\%$ in carbonates to $\sim 18\%$ in quartz (Primak 1958). A complete study on this topic can be found in (Denisov, Dubrovskii, and Solovyov 2012; Le Pape, Alsaid, and Giorla 2018). Expansion is anisotropic along the initial crystalline axis (Denisov, Dubrovskii, and Solovyov 2012). RIVE kinetics are affected by the irradiation temperature causing thermal annealing (Bykov et al. 1981). Aggregates (i.e., rocks) are assemblages of minerals of varied chemical compositions and crystal orientations. Incompatible RIVEs cause the formation of voids and cracks, leading to a degradation in the engineering properties of concrete aggregates and, subsequently, concrete (Hilsdorf, Kropp, and Koch 1978; Seeberger and Hilsdorf 1982; Field, Remec, and Le Pape 2015). Whereas there is consensus about the existence of the fast-neutron damage mechanism in rock-forming minerals, the understanding and models developed to estimate rock-forming minerals' RIVE are based on post-irradiation examination of specimens irradiated in test reactors. These irradiation conditions exhibit fast neutron fluxes that are about 2 orders of magnitude higher than the expected flux in pressurized water reactors (PWRs): seeTable 8. The same comment can be made about the gamma dose in some cases.

Recent post-irradiation dimensional change measurement conducted on two types of aggregates showed important differences in RIVE after irradiation at comparable fast neutron fluence and irradiation temperatures but different fast neutron fluxes. The details of these results—obtained from experiments conducted by the Japan Concrete Aging Management Program (JCAMP) in the JEEP-II reactor and by the centrum výskomu ŘeŽ (CVR) in the LVR-15 reactor—are detailed later in this report. That the fast neutron flux is even lower in PWRs raises questions about the amplitude of the actual RIVE occurring in the CBS over extended operation. It appears that lower expansion is observed when the fast neutron flux decreases.

To support long-term performance analysis of irradiated concrete in light-water reactors (LWRs), predictive models are essential. The Microstructure Oriented Scientific Analysis of Irradiated Concrete (MOSAIC) code, developed by the Light Water Reactor Sustainability (LWRS) Program, addresses this specific need. One of the primary advantages of MOSAIC is its capability to accurately simulate high-fidelity microstructures, including the representation of rock-forming minerals with characteristic sizes typically around 100 μm or smaller. This allows MOSAIC to simulate the radiation-induced expansion of rock and concrete specimens based solely on knowledge of the mineral phases present in the materials under study.

This unique capability is made possible through MOSAIC's linkage with the Irradiated Minerals Aggregate and Concrete (IMAC) database, which contains a comprehensive collection of information and properties of both pristine and irradiated rock-forming minerals. Specifically, the IMAC database includes an extensive

dataset of RIVE data derived from the literature. However, it is important to note that most of these data were obtained from minerals irradiated in test reactors, where they were subjected to high fast neutron fluxes. The exact neutron fluxes during these irradiation experiments, typically in the range of $\sim 10^{12}$ to possibly $\sim 10^{13}$ n·cm^{-2} and above, significantly exceed those encountered in LWRs operations.

This disparity raises concerns about the reliability and relevance of MOSAIC's predictive capabilities for in-service expansion under LWR conditions.

In this work, we pursued two objectives:

1. First, we expanded on the work documented in the LWRS report titled "Validation of MOSAIC-3D Capabilities" (ORNL/SPR-2023/2947) to include the simulation of two well-characterized concrete specimens irradiated in both the LVR-15 and the JEEP-II reactors.
2. The second objective was to formulate hypotheses regarding the origin of the observed neutron flux effects through a literature review of various irradiation sources and by reassessing data on irradiated rock-forming minerals.

2. MOSAIC SIMULATIONS

2.1 CONCRETE

Two aggregates sourced in Japan of varied silica content were used for the fabrication of concrete specimens irradiated in the Institutt for energiteknikk (IFE) JEEP-II test reactor (Kjeller, Norway) by the JCAMP and in the LVR-15 reactor (Husinec, Czechia). The nature and origin of the aggregates are reported in Table 1. The first aggregate GA/F was initially identified as a high-content silica tuff (i.e., consolidated volcanic ash). While tuff often constitutes either igneous or sedimentary light porous rock, aggregate GA appears very compact with no apparent porosity. Later, its classification was modified to metachert by the JCAMP team. It contains more than 90% of quartz (SiO_2) in the form of fine grains.

The second aggregate, GB/E, is categorized as a silicate-bearing sandstone. Its quartz content is 47%. The other constitutive minerals are tectosilicates such as feldspars, predominantly in the form of albite ($NaAlSi_3O_8$, plagioclase) and microcline ($KAlSi_3O_8$, alkali-feldspar), as well as phyllosilicates such as micas, chlorites and clays. Chlorites can be described by the following four end-members based on their chemistry via substitution of the following four elements in the silicate lattice. Magnesium, iron, nickel, and manganese: clinochlore, $(Mg_5Al)(AlSi_3)O_{10}(OH)_8$; chamosite, $(Fe_5Al)(AlSi_3)O_{10}(OH)_8$; nimite, $(Ni_5Al)(AlSi_3)O_{10}(OH)_8$; and pennantite, $(MnAl)_6(SiAl)_4O_{10}(OH)_8 \cdot (MgFeNiMn)_5Al(Si_3Al)O_{10}(OH)_8$, [Si] = 14%. Illite (clay) is structurally quite similar to muscovite, with slightly more silicon, magnesium, iron, and water, and slightly less tetrahedral aluminum and interlayer potassium (elemental markers: K, Al, Mg, Fe and Si). Its chemical formula is $(KH_3O)(AlMgFe)_2(SiAl)_4O_{10}[(OH)_{2(}H_2O)]$, although considerable ion (isomorphic) substitution can occur. Sericite corresponds to very fine, ragged grains of paragonite, muscovite, and illite. Thus, phyllosilicates are quite complex and subject to various atom substitutions. Their behavior under neutron irradiation remains poorly studied, and RIVE data are scarce and limited to biotite and muscovite (i.e., micas) (Denisov, Dubrovskii, and Solovyov 2012). In the simulation presented in this report, it was assumed that all phyllosilicates can be represented by muscovite.

The mineral compositions estimated by x-ray diffraction (XRD) Rietveld analysis are provided in Table 2.

Table 1. Irradiated aggregates' types and origins.

Label	Type	Origin
GA / F	Altered tuff / Crushed	Aichi prefecture
GB / E	Felsic sandstone / Gravel	Shinozuka prefecture

Table 2. XRD Rietveld analysis of the aggregates-forming minerals (Maruyama et al. 2017). The range of variation of the volume fractions is estimated at ±1.5%. Qz: quartz, Ab: albite, An: anorthite, Ano: anorthoclase, Or: orthoclase, Mc: microcline, Chl: chlorite, Ilt: illite, Ser: sericite, Bt: biotite, Cal: calcite, Dol: dolomite, Py: pyrite. Abbreviations according to Whitney and Evans (2010). † The remaining phase was classified as amorphous by Maruyama et al. (2017).

		feldspars					phyllosilicates				carbonates		
	Qz	Ab	An	Ano	Or	Mc	Chl	Ilt	Ser	Bt	Cal	Dol	Py
GA / F	0.92	<0.01	0.02	<0.01	<0.01	0.05			<0.01				
GB / E	0.47	0.24	0.07			0.05	0.03	0.04	0.10				

2.2 MICROSTRUCTURE GENERATIONS

Microstructure generation was completed in two stages. First, randomly shaped polyhedrons corresponding to a given aggregate size distribution were placed in a representative volume of concrete. The `XML` output is a MOSAIC particles map containing a single mineral phase per particle. Second, each particle was subdivided into sub-particles. Each sub-particle corresponds to a specific mineral present in the aggregate composition.

The first part of the generation process was explained in the LWRS report titled "Validation of MOSAIC-3D Capabilities" (ORNL/SPR-2023/2947). The approach is explained below for the sake of completeness.

2.2.1 Generation of Coarse Homogeneous Aggregate

Synthetic 3D microstructures were generated using the `pyCMG` (Holla et al. 2021; Vu et al. 2021; *Concrete Mesostructure Generation Using Python — PyCMG 1.0 documentation,*) software. `pyCMG` is an open-source Python-based code used to generate virtual concrete microstructures. The code creates randomly shaped polyhedra and places them at random locations and orientations within a periodic representative volume element (RVE). Polyhedra are generated by sampling from an inclusion (i.e., aggregate or pore) family given a number of parameters. The polyhedron starts as a box of voxels with the same inclusion family dimensions, and then the polyhedron is made into its final shape by being successively intersected with a number of cutting planes without changing its bounding box dimensions.

Parameters that govern the generation process are as follows.

- Bounding box dimensions (a, b, and c), which will be maintained as fixed during random cutting.
- Volume fraction of the family V_{fi}. Based on the mean particle dimensions, this is computed using the particle size distribution (PSD) of the concrete to be simulated.
- Number of cuts n_{cuts} . This controls the angularity of the shape, where 0 results in a cube, and the larger the number, the more the shape resembles a voxelated ellipsoid (or a sphere if $a = b = c$).
- RVE size (X, Y, Z) in arbitrary units and its resolution (r_x, r_y, r_z).
- Inclusions volume fraction V_f, which is the volume fraction of all inclusions (i.e., particles and pores).

The placement follows the procedure provided below:

1. Inclusion families are arranged in a descending order based on their maximum particle dimension (max[a,b,c]).
2. For each family, a particle is generated by cutting the bounding box using randomly oriented planes successively until the n_{cuts} is reached.
3. Random placement is then attempted, in which a random position is selected and a random rotation matrix is applied to the particle. If all particle voxels were not occupied previously, then the particle is added to the generated volume, and its volume is subtracted from the family volume fraction.
4. If all particle voxels were occupied, then another trial is made using the same generated particle but with a different location and orientation (Step 3) until the number of trials is reached. If there is no success, then another particle shape is generated (Step 2), and then its intersection is checked. This process is repeated until the volume fraction of the family is fully represented. An attempt counter is used to make sure that there are no endless loops.
5. Steps 2 through 4 are repeated for each particle family until the entire volume fraction is exceeded.

Using pyCMG, a very fine microstructure was created. The fine RVE was 60 mm^3 in volume and had a voxel size of 0.15 mm^3, which results in 400^3 voxels in total. The volume fractions of aggregate and voids were 0.672 and 0.033, respectively, so the total inclusion volume fraction is 0.705. The aggregate and void families and their corresponding parameters are listed in Appendix A, Table 12. Note that the volume fractions are relative to the total inclusion volume fraction (i.e., the sum of aggregate and voids), which totals to 1.

After generating the fine microstructure, voxel averaging was performed to generate coarser versions of the same microstructure. Each set of 8 voxels (2 in each Cartesian direction) in the finer microstructure was merged to form 1 voxel in the coarser one. This operation was performed three times to generate 200^3, 100^3, and 50^3 voxel microstructures. In this work, only the 100^3 and 50^3 voxel microstructures were used in the MOSAIC simulations. The volume fractions of aggregates models in the 50^3 and 100^3 voxel microstructures are 0.446 and 0.550, respectively.

2.2.2 Generation of Heterogeneous Aggregate

MOSAIC microstructures are defined in XML files containing varied particles. A *particle* in the context of MOSAIC is a set of pixels or voxels, generally contiguous, that share the same attributes, such as the phase and the crystalline orientation. However, non-contiguous voxels can also define a particle. Thus, a practical approach to obtain heterogeneous aggregate is to scan all its forming voxels and to probabilistically assign each of them to a specific phase. The phase assignment probability is defined by the mineral composition of the aggregate, which can be obtained from XRD–Rietveld analysis. The implementation of the particle subdivision methods was performed using the XML parser embedded in the scientific code *scilab*. Each aggregate particle is duplicated p times, where p is the number of minerals present in the aggregates, and a specific mineral is assigned to each of the duplicated particles. The volume fractions of each minerals derived from XRD–Rietveld analysis reads $f_{j\leq p}$. A random probability ϖ is generated from a uniform distribution given by $\mathcal{U}(0, 1)$. The mineral phase assignment to the k^{th} mineral obeys the relation $\sum_1^k f_j \leq \varpi < \sum_1^{k+1} f_j$. Table 3 shows that the average minerals contents in the synthetic aggregates match the XRD–Rietveld analysis. The minerals contents vary for each aggregate. The synthetic microstructures are presented in Table 7. The different minerals are presented with the following color scale ranging from blue (1) to red (quartz): 1: cement paste; 2: void; 3: phyllosilicate (mica, chlorite, clay); 4: microcline; 5: anorthite (GB) or anorthoclase (GA); 6: albite; and 7: quartz.

Table 3. Comparison of minerals' volume fractions obtained by XRD–Rietveld analysis and by probabilistic assignment in the MOSAIC microstructures.

			GA		
	Qz	Ab	Ano/An	Mc	Phyl
XRD	0.918	0.008	0.023	0.031	0.009
50^3	0.917	0.008	0.023	0.041	0.011
100^3	0.918	0.008	0.023	0.041	0.010
			GB		
XRD	0.471	0.236	0.072	0.046	0.179
50^3	0.473	0.237	0.071	0.046	0.173
100^3	0.471	0.236	0.072	0.046	0.175

Table 4. 3D MOSAIC microstructures.

GA	GB
$50 \times 50 \times 50$	
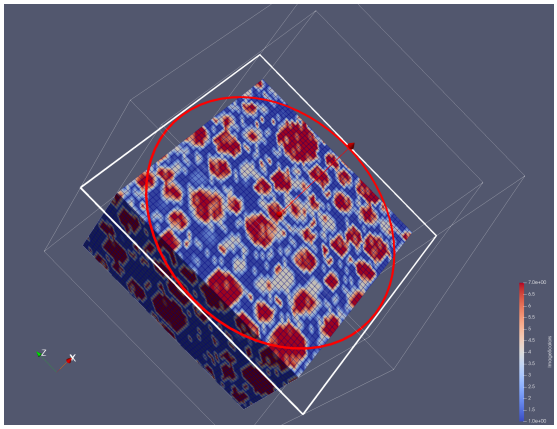	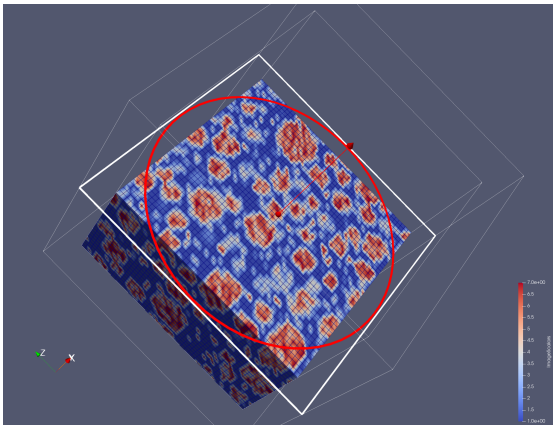
$100 \times 100 \times 100$	
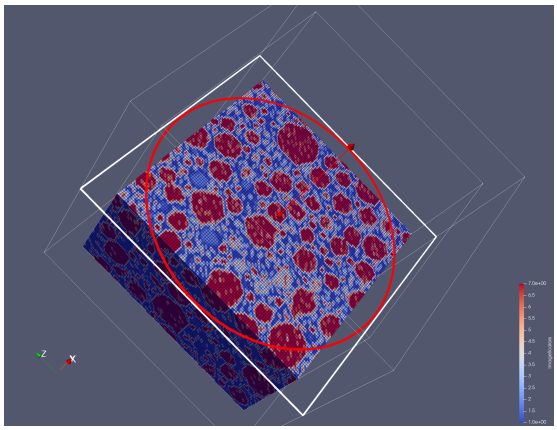	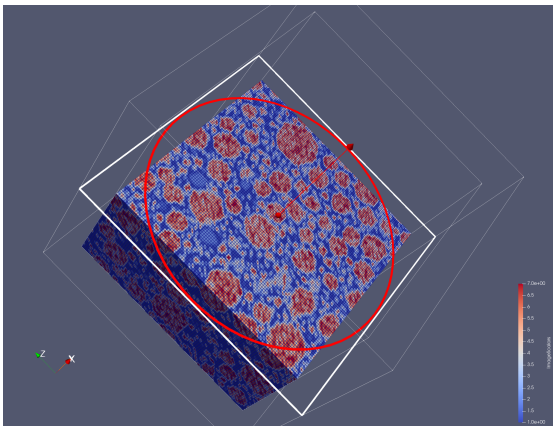

2.3 MATERIALS PROPERTIES

2.3.1 Elastic Properties

2.3.1.1 Rock-Forming Minerals

Rock-forming minerals have generally anisotropic elastic properties because of their crystalline structures. At the modeling scale of this study, minerals are considered isotropic. For each mineral, its apparent isotropic properties are derived from the homogenization of a polycrystalline assemblage of minerals distributed in random orientations. The results of the homogenization are presented in Table 5.

Using homogenization techniques described in Le Pape, Sanahuja, and Alsaid (2020), the Young modulus of aggregates GA and GB can be estimated at 100.8 and 99.6 GPa, respectively. These estimates assume that the minerals are perfectly crystalline, contain no defects, and are perfectly bonded at the grain boundaries. The presence of defects in the form of micro-pores and interfacial defects at the grain boundaries caused by weathering and rock crushing to create aggregates reduces the effective Young's modulus ($\tilde{E}$) of the aggregates. From a modeling point of view, the simplest strategy is to reduce the apparent Young's moduli of the constitutive minerals by a factor equal to $\tilde{E}/E \sim 0.6$. The reduced apparent Young's moduli of the constitutive minerals range between ~ 41 and ~ 66 GPa—see the last column in Table 5. Their respective Poisson ratios were assumed to be unchanged.

Table 5. Elastic properties of minerals and aggregates. E: Young modulus, ν: Poisson ratio, k: bulk modulus, μ: shear modulus, $\tilde{E}$: reduced Young modulus. All values are given in GPa except for the Poison ratio. ($*$: values for muscovite).

mineral	E	ν	k	μ	$\tilde{E}$
quartz	101.4	0.06	38.2	47.9	60.8
albite	91.7	0.25	61.2	36.7	55.0
anorthite	109.7	0.29	87.5	42.5	65.8
anorthoclase	74.6	0.31	64.4	28.5	40.8
microcline	83.5	0.27	59.7	32.9	50.1
phyllosilicate$*$	103.9	0.22	62.0	42.6	62.3
aggregate	E	ν	k	μ	$\tilde{E}$
GA	100.8	0.08	40.0	46.7	60.5
GB	99.6	0.17	50.9	42.4	59.8

During neutron irradiation, voids and cracks form in aggregate, resulting in the loss of their elastic moduli. Post irradiation scanning electron microscopy (SEM) observations [unpublished data collected by D. Arregui Mena at ORNL] show diverse cracking patterns, including initiation around large quartz grains, propagation along grain boundaries, and transgranular cracks in feldspars. Explicit modeling of these concurrent cracking modes is complex. In previous 2D MOSAIC simulations of irradiated aggregates, Cheniour et al. (2022) modeled the grain boundaries with fine 1-pixel interfaces separating adjacent minerals. Using a damage model at these interface elements, grain boundary cracking could be explicitly represented. However, this approach required that the pixel (or voxel) size in the aggregate microstructure be small enough to permit scale separation between the interfacial zone and the grains. In the proposed 3D simulations, the irradiation-induced loss of modulus is accounted for using post-irradiation ultrasound velocity measurement collected by ORNL on the JCAMP aggregate specimens. Figure 1 provides a comprehensive summary of the ratio of irradiated to pristine Young's modulus of diverse aggregates as a function of the RIVE. This figure includes both data collected by Denisov, Dubrovskii, and Solovyov (2012) (gray marks) on mainly igneous rock specimens and data obtained on JCAMP aggregate (in red circles, aggregate GA/F and in brown circles, aggregate GB/E). The irradiated moduli of the JCAMP aggregates decrease at a lower rate than do the igneous rocks reported by Denisov, Dubrovskii, and Solovyov (2012). The loss of modulus for aggregate GA/F can be approximated by a linear trend: $E^*/E_0 \simeq 1 - 0.054\varepsilon^*$. The JCAMP sandstones exhibit a more important reduction of the modulus at low RIVEs. The general trend can be modeled using this expression: $E^*/E_0 \simeq [1 + 0.172(\varepsilon^*)^{1.09}]^{-1}$

In the MOSAIC simulation presented in this report, varied irradiation conditions are considered. Because the data points corresponding to the highest RIVEs (ranging between 8% and 12%) in Figure 1 were obtained from specimens extracted from capsule PPT-E (See Section 2.4.1.1 for details), these data points are considered unreliable. Thus, the lower bound values for the loss of Young's modulus of aggregate GA/F and GB/E were determined from the data points collected on the specimens irradiated in capsule PPT-D, corresponding to RIVEs ranging between approximately 2% and 5%. The corresponding lowest residual irradiated modulus for aggregates GA/F and GB/E are $\simeq$ 77.5% and $\simeq$ 60% of their pristine moduli, respectively.

2.3.1.2 Cement Paste

The cement paste was assumed to be homogeneous and its elastic properties isotropic. The Young's modulus and Poisson ratio were assumed to be equal to 12 GPa and 0.2, respectively (Maruyama et al. 2017).

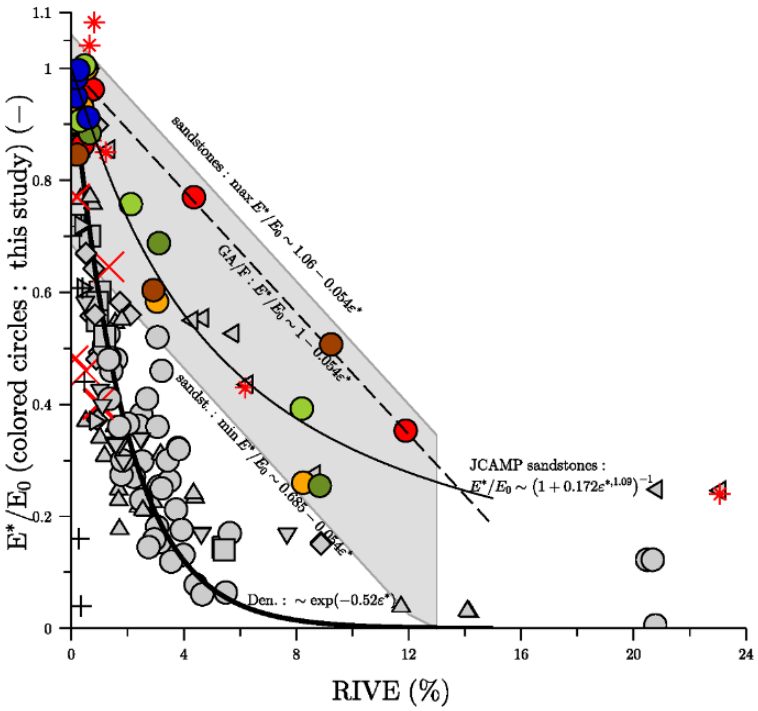

Figure 1. Loss of Young's modulus of irradiated rocks. Colored circles: JCAMP data; Gray/red marks: literature data from Denisov, Dubrovskii, and Solovyov (2012); upward triangles: albitite; left triangles: aleurolite; diamonds: diabase; circles: granite; squares: hornblendite; ×: limestone; right triangles: magnesite; downward triangles: pyroxenite; ∗: sandstone and +: siderite.

2.3.2 Radiation-Induced Volumetric Expansion of Aggregate-Forming Minerals

Radiation-induced expansion is associated with a gradual increase in the volume of defects and the distortion of the crystalline network. RIVE of the constitutive minerals was assumed to be isotropic and was modeled using empirical models (Le Pape, Alsaid, and Giorla 2018) derived from accelerated test data mostly documented in Denisov, Dubrovskii, and Solovyov (2012). Those empirical models assume that RIVE, ε^* is a function of the "fast-neutron" fluence (Φ at $E > 10$ keV) and the irradiation temperature T. Most silicates exhibit a sigmoidal evolution of RIVE with increasing fluence at constant temperature.

From a physical point of view, only rock-forming minerals are subject to RIVE. From a modeling point of view, it is necessary to assume RIVE in the cement paste to account for the fine aggregates lost during the synthetic microstructure generation or those that are too small to be represented by single voxel particles. Analytical expressions provided in Le Pape, Field, and Remec (2015) show that the volumetric expansion of irradiated concrete $\langle \varepsilon^* \rangle$ has the following bounds:

- *Lower bond*:

$$\langle \varepsilon^*_{lb} \rangle = f_a \varepsilon^* + (1 - f_a)\varepsilon_{sh} \tag{1}$$

- *Upper bond*:

$$\langle \varepsilon^*_{ub} \rangle = 2f_a/(1 + f_a)(\varepsilon^* + \alpha \Delta T) \tag{2}$$

In Eqs. (1–2) f_a, ε^*, ε_{sh}, and $\alpha \Delta T$ are the volume fraction of aggregate, the aggregate RIVE, the paste shrinkage, and the thermal expansion of aggregate. Thus, underestimating the volume fraction of aggregates leads to significant error. To correct this underestimation, the contribution of fine aggregate to the expansion of concrete must be included as an additional expansion occurring in the cement paste. Let $\tilde{f}_a$ be the volume fraction of aggregates present in the model. The equivalent volumetric expansion ($\tilde{\varepsilon}^*$) caused by fine aggregate in the cement is governed by the expression $f_a \varepsilon^* \simeq \tilde{f}_a \varepsilon^* + (1 - \tilde{f}_a)\tilde{\varepsilon}^*$ Hence, the volumetric expansion ($\tilde{\varepsilon}^*$) reads

$$\tilde{\varepsilon}^* \simeq \frac{f_a - \tilde{f}_a}{1 - \tilde{f}_a} \varepsilon^*,$$

with $\tilde{f}_a \leq f_a \leq 1$. The aggregate's RIVE can be estimated from its chemical composition: $\varepsilon^* \simeq \sum f_i \varepsilon^*_i$, where f_i and ε^*_i are the volume fraction of mineral i in the aggregate and its specific RIVE. In concrete Con-A, aggregates contain 92% quartz, which dominates the aggregate's RIVE. Therefore, a good approximation of the aggregate GA/F RIVE is $\simeq 0.92\varepsilon^*_{Qz}$. The equivalent volumetric expansion of fine aggregate embedded in the cement paste can be estimated by modifying the maximum amplitude of quartz's RIVE model—see Table 6.

Table 6. Concrete Con-A: apparent maximal RIVE of the fine aggregates embedded in the cement paste.

microstructure	agg. vol. frac. f_a	app. vol. frac. $\tilde{f}_a$	app. RIVE amplitude $\tilde{\varepsilon}^*_{max}$
50^3 Con-A	0.705	0.446	0.076
100^3 Con-A	0.705	0.550	0.0564

2.3.3 Damage in the Cement Paste

Anisotropic damage governed by a unique scalar variable varying from 0 to 1 is implemented in MOSAIC, although "the algorithm could be extended to other forms of damage or irreversible phenomena including

orthotropic damage or visco-plasticity" (Giorla, Le Pape, and Dunant 2017). Damage is calculated by considering the stress-strain curve of the material to be the failure envelope. The stress strain curve can be used to represent brittle materials, pseudo-plastic materials, linear softening, or exponential softening (Giorla and Le Pape 2015; Giorla, Le Pape, and Dunant 2017). The aggregates' RIVE causes the development of stresses in the cement paste. The stored mechanical energy eventually needs to be dissipated through cracking or viscous strains. Whereas these competitive mechanisms require a coupled damage–creep model implemented in MOSAIC (Giorla, Le Pape, and Dunant 2017), this coupling is computationally expensive. In this study, a simplified approach was adopted, assuming that the elastic modulus of the hardened cement paste (HCP) corresponds to a "delayed" modulus: $\tilde{E} \sim E/3$. This factor of 3 assumes that the creep deformation is twice as large as the instantaneous deformation. This factor was applied to all elastic constants of the elastic tensor $\tilde{\mathbf{C}}_e$. Hence, the MOSAIC solver computes the solution to the following equation:

$$\sigma = (1 - d)\tilde{\mathbf{C}}_e : [\varepsilon - \varepsilon^*], \tag{3}$$

where $\mathbf{C}_e$ is the delayed elastic stiffness tensor of the HCP, ε is the total strain, and ε^* is the imposed strain (i.e., RIVE).

2.4 IRRADIATION CONDITIONS

2.4.1 Accelerated Irradiation in Test Reactors

2.4.1.1 JEEP-2

The detailed description of the irradiation experiments can be found in Maruyama et al. (2017). The IFE Kjeller JEEP-2 reactor typically operates at a flux range of 0.05 to 1.0 $\times 10^{13}$ n·cm^{-2} s^{-1} (fast neutrons). The low flux is advantageous for testing concrete due to its low gamma heating, which is estimated to be in the range of 0.03 to 0.2 W g^{-1}. Four irradiation experiments were conducted in four separate physical property tests (PPTs) capsules named PPT-B, PPT-C, PPT-D and PPT-E, reaching fast neutron fluence range of 0.67–0.83 $\times 10^{19}$ n·cm^{-2}, 1.23–1.48 $\times 10^{19}$ n·cm^{-2}, 3.97–4.77 $\times 10^{19}$ n·cm^{-2}, and 7.97–9.60 $\times 10^{19}$ n·cm^{-2}, respectively, at $E > 0.1$ MeV. Fluence ranges are caused by the spatial variation of the neutron flux along the height of the capsule hosting the specimens stack. Because of unexpected RIVE, capsule PPT-E cracked and reactor coolant leaked in. The JCAMP team advised caution when using the data obtained from this test. Based on the information provided in Maruyama et al. (2017), the average fast neutron flux in capsule PPT-C is estimated to be around $\sim 3.6 \times 10^{12}$ n·cm^{-2} s^{-1} ($E > 0.1$ MeV). To obtain the fast neutron fluence at $E > 10$ keV, fluence at $E > 0.1$ MeV is multiplied by ~ 1.6 in JEEP-II PPT capsules. The gamma dose rate is about 300 kGy h^{-1}.

2.4.1.2 LVR-15

This irradiation experiment was conducted for the U.S. Nuclear Regulatory Commission (NRC) to study the effects of irradiation on the bond strength of steel reinforcement embedded in concrete. The experiment also included the irradiation of plain concrete specimens made from the same constituents as those used in the previous experiment conducted at IFE for the JCAMP.

The final average fluence is 1.12×10^{19} n·cm^{-2} ($E > 0.1$ MeV). The corresponding minimum and maximum fluences are, respectively, 0.87×10^{19} n·cm^{-2} and 1.23×10^{19} n·cm^{-2}. To obtain the fast neutron fluence at $E > 10$ keV, the fluence at $E > 0.1$ MeV was multiplied by 1.23–1.24 in the XK1 position.

2.4.2 In-Service Irradiation in PWRs

In-service irradiation of the CBS varies with reactor type, core design and modification, and energy factor. Estimates of the fast neutron fluence at 80 effective full-power years (EFPYs) can be found in (Esselman and Bruck 2013) for LWRs operated in the United States at the time. The fluences at the surface of the CBS were extrapolated from reactor pressure vessel (RPV) surveillance data. Neutron fluence extrapolation ranges from $> 10^{19}$ to $< 7 \times 10^{19}$ n·cm^{-2} ($E > 0.1$ MeV) at projected 80 EFPYs across the varied United States' two-loop PWRs. The corresponding ranges for three-loop and four-loop reactors are $> 5 \times 10^{19}$ to $< 7 \times 10^{19}$ n·cm^{-2} and $> 1.5 \times 10^{19}$ to $< 3.5 \times 10^{19}$ n·cm^{-2}, respectively. The average flux across all US PWRs is estimated to be between $>\sim 4 \times 10^{9}$ and $<\sim 2.75 \times 10^{10}$ n·cm^{-2} s^{-1} ($E > 0.1$ MeV). Gamma doses are provided for 2 two-loop PWRs and a three-loop PWR studied by ORNL and TransWare Enterprises and range between around 50 and 125 MGy at 80 EFPYs, corresponding to average gamma dose rates of 0.07 and 0.18 kGy h^{-1}, respectively. Temperature in the CBS during operation is estimated to be between 45 and 65 °C.

2.5 SIMULATIONS

2.5.1 Studied Scenarios

The MOSAIC simulations performed in this work include the following scenarios:

1. Increasing fast neutron fluence from 0 to about 7×10^{19} n·cm^{-2} ($E > 10$ keV) or lower pending solver convergence.
2. Two bounding irradiation temperatures at 45 °C and 72 °C, corresponding to conditions in the JEEP-II and LVR-15/XK1 experiments, respectively. The proposed temperature range covers expected LWR operating temperatures.
3. The effects of irradiation on the Young's modulus of aggregate were studied considering bounding values: no reduction of the pristine modulus or lower bound value. The corresponding simulation results are identified with the letter (P) for *pristine* and (R) for *reduced*.
4. The cement paste may or may not experience mechanical damage caused by RIVE-induced stresses. Simulations were conducted with and without damage. When mechanical damage is activated, the simulation results are identified with the letter (D) for *damage*.

In summary, the anticipated lower bound scenario aims to achieve a low RIVE estimate. This is done by using the highest aggregate Young's modulus (i.e., the pristine value, ignoring irradiation-induced loss of modulus) and the highest irradiation temperature (72 °C) to minimize aggregate expansion. The anticipated upper bound scenario assumes a reduction in the aggregate Young's modulus of 22.5% and 40% for aggregates GA/F and GB/E, respectively, as explained in Section 2.3.1.1. The Young's modulus of each aggregate-forming mineral in aggregates GA/F and GB/E was modified using the same reduction parameter. The irradiation temperature for this scenario is 45 °C.

2.5.2 Experimental Data

The dimensional changes obtained for the MOSAIC 3D simulations are compared with the data collected by the JCAMP (irradiation in the JEEP-II reactor) and those collected by Oak Ridge National Laboratory (ORNL) (LVR-15 reactor); see Section 2.4 for details on the irradiation conditions.

2.5.2.1 JEEP-II

The dimensional changes (length and diameter) of the concrete specimens are presented in Fig. 37(b) of Maruyama et al. (2017). The data were digitized using the free utility software *Engauge Digitizer*. Note that in the original article, the fluence values are provided for energy higher than 0.1 MeV. Fluence values were corrected by a factor of ×1.692 to obtain estimates at energy higher than 10 keV. This value was determined from the analysis of the energy lethargy spectrum provided by Pr. Maruyama [private communication]. The data are presented using red filled circles in the figures on this report.

Table 7. Summary of the MOSAIC simulations completed for this study.

Irr. Temp. (°C)	Microstructure 50^3	100^3
Concrete Con-A		
45	(P), (R), (D)	(R)
72	(P), (R), (D)	(R)
Concrete Con-B		
45	(P), (R)	
72	(P), (R)	

2.5.2.2 LVR-15

The specimens' dimensions were obtained using the Micro-Vu Vertex system insulated against vibration and equipped with 3D coordinate measuring machine computer numerical control, a measuring camera equipped with a codebook, distribution and comparator chip, and a touch probe placed in the feeder. The dimensions were measured using the touch probe. Marks were drawn on the specimens to ensure that post-irradiation measurement locations match the pre-irradiation data. The pre- and post-irradiation diameters were measured at three elevations and at four angles on hollow cylindrical concrete specimens (40 mm in height and 40 mm in height). The experiment included three specimens made of concrete Con-A and three specimens made of concrete Con-B. The data are presented as the mean value (blue square marks), the min./max. amplitude (blue thin vertical lines), and the $\pm\sigma/2$ (blue thick vertical lines), where σ is the standard deviation calculated from twelve measurements. Because the specimens were stacked in a $\approx$ 670 mm arrangement, the fast neutron flux at the end of the irradiation experiment varied slightly for each specimen.

2.5.3 Other Analytical and Simulation Estimates

2.5.3.1 Analytical Model

Concrete RIVE estimates are also calculated in Eq. (1) and Eq. (2), which provide a lower and an upper bound, respectively (Le Pape, Field, and Remec 2015). In those expressions, the contribution of the thermal expansion is negligible to $T \leq 72$ °C. The cement paste shrinkage is estimated to be under 0.1%; See Fig. 40(a) of Maruyama et al. (2017). Concrete RIVE estimates are plotted using dashed lines.

2.5.3.2 MOSAIC 2D Simulations

In a previous study (Le Pape et al. 2019), a realistic 2D microstructure of concrete Con-A was created by combining petrography, energy-dispersive x-ray spectroscopy (EDS), and micro x-ray fluorescence (m-XRF) data. The obtained phase map is presented in Figure 2. The result of the MOSAIC 2D simulation for concrete Con-A is plotted using thin solid lines. No simulations were conducted on concrete Con-B.

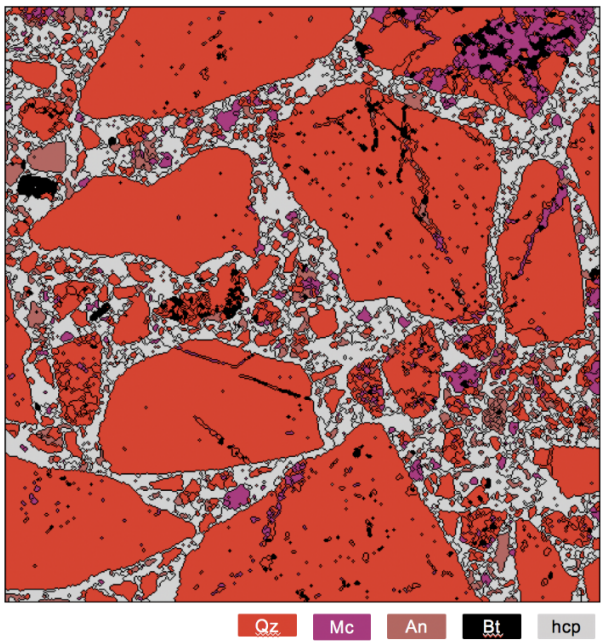

Figure 2. Concrete Con-A MOSAIC microstructure reconstructed from m-XRF elemental maps. Qz: quartz, Mc: microcline, An: anorthite, Bt: biotite and hcp: hardened cement paste.

2.5.4 Results

Figure 3 and Figure 4 present the RIVE evolution against increasing fast neutron fluence ($E > 10$ keV) for irradiation temperatures of 72 °C (Left) and 45 °C (Right) for concrete Con-A and Con-B, respectively. The MOSAIC 3D simulation results are plotted using thick solid lines. A diamond mark shows the final computed results before the solver stopped converging. (P) corresponds to the simulation assuming a pristine (i.e., not affected by irradiation-induced damage) aggregate. R shows the results assuming a reduced Young's modulus for the aggregate. (P) and (R) results were obtained on the 50^3 microstructures. (R100) corresponds to the 100^3 microstructures.

The analysis of FIG leads to the following observations:

1. MOSAIC 3D simulations compare well with the experimental length change obtained by the JCAMP team (JEEP-II reactor, irradiation temperature 72 °C, fast neutron flux $\sim 3.6 \times 10^{12}$ n·cm^{-2} s^{-1} ($E > 0.1$ MeV). However, MOSAIC 3D simulations overestimate the length measured on specimens irradiated in the (LVR-15 reactor, irradiation temperature 45 °C, fast neutron flux $\sim 3.6{\times}10^{11}$ n·cm^{-2} s^{-1} ($E > 0.1$ MeV).
2. MOSAIC 3D simulations did not converge for a fluence of $\gtrapprox 6.5 \times 10^{19}$ n·cm^{-2} and a length change of $\gtrapprox 0.675\%$ for simulations conducted without a damage model to represent cracking in the cement paste. When a damage model is introduced, convergence is difficult to obtain even at fluence $\approx 10^{19}$ n·cm^{-2}.
3. (R), (P), and (D) cases found very close length change estimates.
4. Length changes obtained from MOSAIC 3D simulations and the analytical expressions from Eq. (1) and (2) are comparable.
5. MOSAIC 2D underestimates the length change of concrete Con-A specimens irradiated in JEEP-II.

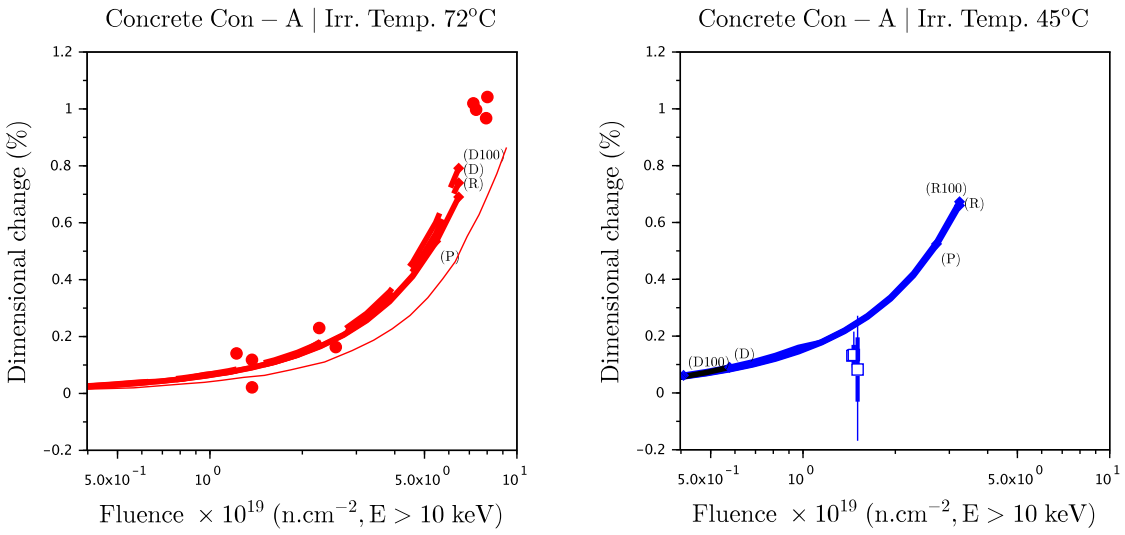

Figure 3. Evolution of the dimensional change of concrete Con-A with fast neutron fluence. (Left) Irradiation temperature of 72 °C; experimental data marks from Maruyama et al. (2017) – JEEP-II reactor. (Right) Irradiation temperature of 45 °C; experimental data marks from ORNL study in LVR-15 reactor.

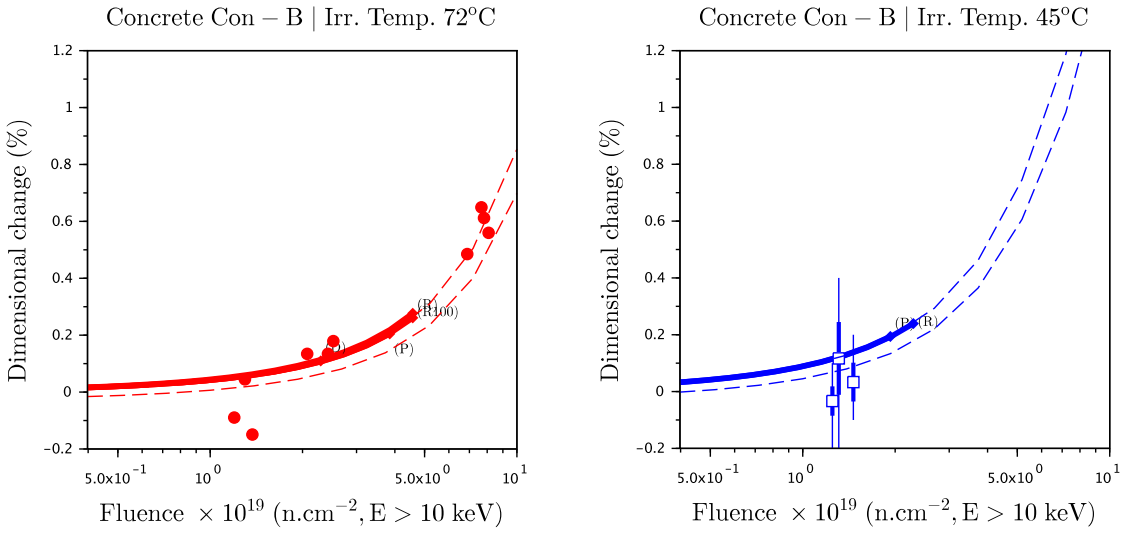

Figure 4. Evolution of the dimensional change of concrete Con-B with fast neutron fluence. (Left) Irradiation temperature of 72 °C; experimental data marks from Maruyama et al. (2017) – JEEP-II reactor. (Right) Irradiation temperature of 45 °C, experimental data marks from ORNL study in LVR-15 reactor.

2.6 SUMMARY OF MAIN FINDINGS

In summary, the length change of irradiated concrete in test reactors is governed by aggregate RIVE. The influence of the pristine of damaged elastic properties of the concrete constituents on concrete RIVE is very limited. It was found that good approximations of the RIVE of concrete Con-A and Con-B can be obtained using either analytical expressions, which use the aggregate RIVE and volume fraction as the main parameters, or 3D MOSAIC simulations based on data obtained from JCAMP irradiation experiments conducted in the JEEP-II reactor.

In a simplified mathematical form, the concrete RIVE can be expressed as

$$\langle \varepsilon^* \rangle \approx g(f_a) \sum f_i \mathcal{F}_i(\Phi, T), \tag{4}$$

where $\langle \varepsilon^* \rangle$ is the concrete RIVE, f_a is the volume fraction of the aggregate, and $\sum_1^n f_i \mathcal{F}_i(\Phi, T)$ is the aggregate RIVE estimated from the weighted contribution of the n minerals' RIVE present in the aggregate. The minerals' RIVEs are calculated as a function of the fast neutron fluence Φ and the irradiation temperature. The parameters governing the function $\mathcal{F}_i$ are mineral dependent and were calibrated on dimensional change obtained mainly from irradiation experiments in Russian reactors (AM, OK-50, BR-5, BR-10 and BOR-60 (Denisov, Dubrovskii, and Solovyov 2012).

Although RIVE values obtained from analytical and 3D MOSAIC simulation results are comparable, both approaches overestimated the dimensional changes of concrete specimens Con-A and Con-B irradiated in the out-of-core XK1 position in the LVR-15 reactor.

The irradiation conditions in the JEEP-II (PPT-C) and LVR-15 (XK1) reactors are detailed in Table 8. The fast neutron fluence at the XK1 position is within the range of the fluence observed in capsules PPT-B and PPT-C in the JEEP-II reactor. If the irradiation temperature at the XK1 position were similar to that of the PPT-B and PPT-C capsules (approximately 72 °C), then it would be expected that the linear changes measured after irradiation in both reactors would be comparable. However, because the irradiation temperature at the XK1 position is lower (approximately 45 °C) than that in the PPT-B and PPT-C capsules, it was anticipated that the aggregate RIVE and, consequently, the concrete's RIVE would be higher in the capsule irradiated at the XK1 position. This phenomenon is documented in Bykov et al. (1981). The post-irradiation dimensional change measured on concrete specimens contradicts this mechanism.

In addition, Figure 5 presents a comparison of the linear expansion of aggregate GA/F after irradiation in the LVR-15/XK1 position (filled blue circles) and the JEEP-II reactor (capsules PPT-B and PPT-C – filled red circles). Additional data provided by Professor Maruyama from the University of Tokyo during the LWRS Program Spring Meeting on April 30 and May 1, 2024, are also plotted. These data were obtained from post-irradiation measurements on similar aggregate specimens that were irradiated in two in-core positions—E10 (filled red squares) and G1 (filled red diamonds)—in the LVR-15 reactor. The dashed lines represent linear trends that provide a rough approximation of the evolution of RIVE with increasing fluence below 2.5×10^{19} n·cm^{-2}. Each line connects the dimensional change data obtained from the three irradiation positions in the LVR-15 reactor: XK1 (blue), E10 (red), and G1 (black). These positions correspond to fast neutron fluxes of 3.6×10^{11}, 4.8×10^{12} and 1.9×10^{13} n·cm^{-2} s^{-1} ($E > 0.1$ MeV for each position, respectively. The data suggest a decrease in the aggregate RIVE with decreasing fast neutron flux.

This result suggests that Eq. (4) is incomplete and needs to include the fast neutron flux, $\dot{\Phi}$, as an additional parameter:

$$\langle \varepsilon^* \rangle \approx g(f_a) \sum f_i \mathcal{F}_i(\Phi, \dot{\Phi}, T). \tag{5}$$

The exact mathematical form of Eq. (5) has yet to be determined.

It should also be noted that the dimensional change observed in specimens irradiated in the JEEP-II reactor at a fast neutron flux of 3.6×10^{12} n·cm^{-2} s^{-1} appears to be consistent with the post-irradiation measurements from specimens irradiated in the LVR-15/G1 position at a flux of 1.9×10^{13} n·cm^{-2} s^{-1}. This apparent discrepancy may be due to differences in irradiation temperatures, which have not yet been communicated by the JCAMP team.

Therefore, it is not currently possible to determine the RIVE of in-service irradiated concrete in LWRs until the effects of fast neutron flux are resolved. However, using the operating fast neutron fluence and temperature in Eq. (4) will provide a conservative estimate.

The following sections explore the possible origins of the observed neutron flux effect by revisiting the literature.

Table 8. Comparison of the irradiation conditions between the JEEP-II reactor (JCAMP experiment) LVR-15 (NRC experiment) and a prototypical PWR. Data taken from Maruyama et al. (2017) and Remec (2013). † Current operation extension.

	JEEP-II/PPT-C[(j)]	LVR-15/XK0[(l)]	PWR[(p)]	ratio[(j/l)]	ratio[(l/p)]
	Fast neutron flux ($\times 10^{11}$ n·cm^{-2} s^{-1})				
$E > 0.1$ MeV	34–36	5.6–6.0	≈0.1–0.2	× ≈ 6	× ≈30–60
	Target fluence ($\times 10^{19}$ n·cm^{-2})				
$E > 0.1$ MeV	1.5	2.0	< 6.0	×0.75	× > 1/3
$E > 10$ keV	2.4	2.3		×1.05	
	Target gamma dose (GGy)				
		0.9–1.3	0.1–0.2		×1/5–1/10
	Gamma heating (W g^{-1})				
	0.04–0.06	0.09	0.02	× ≈0.5	× ≈ 0.2
	Surface-to-center temperature (°C)				
	62–73	58–73	< 65	×0.9–1.1	×0.9–1.1
	Duration (full power year)				
	0.25	≈ 2	< 80†	×1/8	×1/40

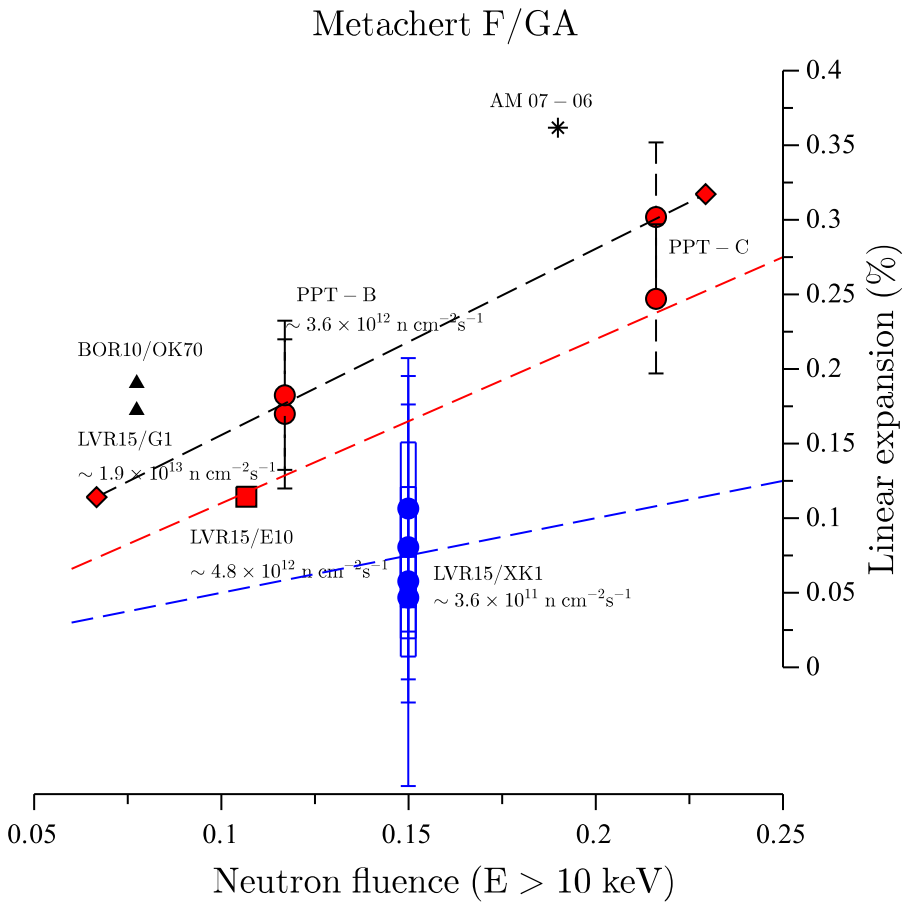

Figure 5. Comparison of radiation-induced linear expansion of aggregate GA/F in various test reactors. Note that fluence values are provided in $\times 10^{20}$ n·cm^{-2}.

3. REVISITING LITERATURE DATA THROUGH UNIFIED DAMAGE PER ATOM ANALYSIS

Bykov et al. (1981) gathered a series of RIVE data from neutron irradiation experiments conducted on quartz mineral specimens in various test reactors. These experiments resulted in different irradiation temperatures, with average values ranging from 300 to 600 °C. The data are provided as post-irradiation RIVEs functions of the fast neutron fluence ($E > 10$ keV up to 50×10^{19} n·cm^{-2}). Isothermal RIVE curves are sigmoidal: see Figure 6. Whereas the final expansion (17.8%) is independent of the irradiation temperature, the RIVE rate decreases with the irradiation temperature. Bykov et al. (1981) attribute this effect to point-defect annealing: "The apparent significant effect of the temperature of irradiation on the radiation expansion of quartz obviously is explained by the annealing of point defects during irradiation, as the other processes which determine the radiation expansion of a material, should not depend significantly on the temperature of irradiation." Importantly, XRD analysis shows that changes in lattice properties and the corresponding volumetric changes are independent of the irradiation temperature, suggesting that the nature of the irradiation defects is comparable.

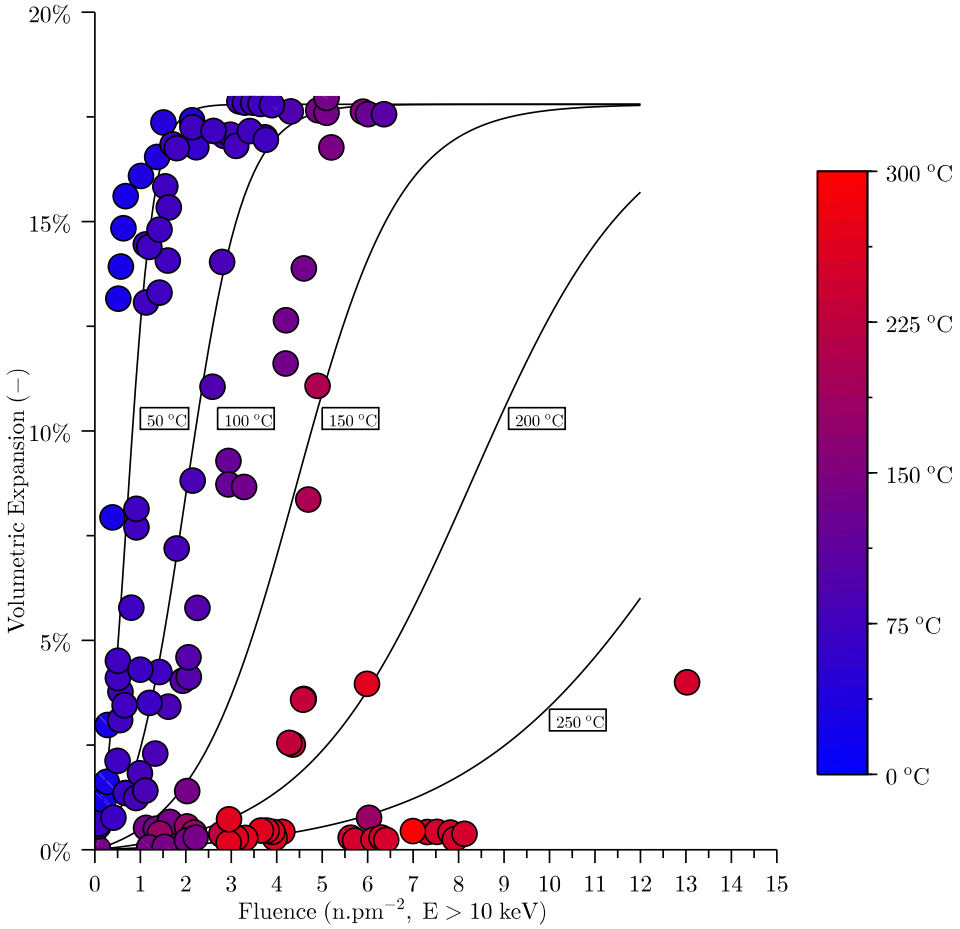

Figure 6. Quartz RIVE (Bykov et al. 1981). The color chart corresponds to the average irradiation temperature. Solid lines: theoretical curves using the expression from Zubov and Ivanov (1966).

The experiments were conducted in varied Russian test reactors and positions, including channels 02-13 and 07-06 of the AM reactor, channel OK-50 of the BR-5 reactor, channel M-1 of the BR-5 reactor, channel OK-70 of the BR-10 reactor and the VEK channels of the BOR-60 reactor. In addition, ORNL conducted an irradiation experiment for the NRC on aggregates provided by JCAMP in the XK1 position of the LVR-15 reactor. One of the two tested aggregates, aggregate GA/F, contains 92% of quartz, which makes it a good candidate for comparison with pure quartz minerals data. As previously explained, the analysis of Russian data led to the development of empirical models for the RIVE of several common rock-forming minerals (Le Pape, Alsaid, and Giorla 2018). The general mathematical form of these empirical equations is given by $\mathcal{F}_i(\Phi, T)$, assuming that the RIVE is governed by the fast neutron fluence, Φ, and the irradiation temperature, T. These parameters are used in the literature to describe the RIVE data and the irradiation condition. Nevertheless, as noted above, these data were obtained in various test reactors.

Remec et al. (2018) proposed a unifying methodology for interpreting irradiation data by calculating displacement per atom (dpa) rates using SPECTER simulations of minerals with varied compositions. In the study presented herein, the Russian and ORNL data were revisited to obtain RIVE as a function of dpas and average irradiation temperature: that is, $\mathcal{F}_i(dpa, T)$.

3.1 TEST REACTORS NEUTRON SPECTRA

Neutron spectra of the Russian reactors are given in Tab. 2.2., p. 32 in Denisov, Dubrovskii, and Solovyov (2012). It should be noted that the neutron fractions had to be re-normalized for the AM reactor and the BOR-60 (VEK channel) reactor, as the sums of the neutron fractions were 1.02 and 1.98, respectively. The neutron fractions are presented in Figure 7 (Left): red line: channels 02-13 and 07-06 of the AM reactor; black thin lines: channels OK-50 and M-1 of the BR-5 reactor; blue line: channel OK-70 of the BR-10 reactor; and green line: VEK channel of the BOR-60 reactor. The thin black lines correspond to the spectrum in the XK1 position of the LVR-15 reactor (Czechia). Two spectra are plotted corresponding to the first and last irradiation cycles K224 and K236. During the removal of an adjacent capsule from the XK0 position after the 8th cycle, the irradiation rig moved by a few inches. This displacement affected the fast neutron flux by a factor of about 30%. However, as observed in Figure 7, it has little effect on the neutron spectrum: the two curves are nearly identical. Note that the energy discretization is finer for the LVR-15 data than it is for the Russian data. Figure 7 (Right) shows the cumulative neutron fraction at $E > E_0$. It can observed that the cumulative neutron spectra are comparable for the OK50 and M1 channels of the BR-5 reactor (black lines) and the channel OK-70 of the BR-10 reactor (blue line). These spectra are *stiffer* than the spectra for the channels 02-13 and 07-06 of the AM reactor and the XK1 position of the LVR-15 reactor (thick black line – cycle K224), which are comparable.

Because it is convenient to express the RIVE data for fast neutron fluence at $E > 10$ keV (Denisov, Dubrovskii, and Solovyov 2012), the corresponding fast neutron fluence reads

$$\frac{\Phi(E > 10 \text{ keV})}{\Phi(E > 0 \text{ eV})} = \frac{\int_{E>10 \text{ keV}}^{+\infty} \varpi(E) dE}{\int_{E>0 \text{ eV}}^{+\infty} \varpi(E) dE} = \xi, \tag{6}$$

where ϖ is the neutron fraction at a given energy level—that is, as characterized by Figure 7 (Left). The values of ξ for the studied reactor positions are provided in Table 9. The fraction of the fluence at energy higher than $E > 10$ keV ranges between $\approx 75\%$ and $\approx 80\%$ in the BR-5 and BR-10 reactors, is about 40% in the AM and BOR-60 reactors, and is close to 30% in the LVR-15 reactor. These values are only correct for the specific channels and positions reported here.

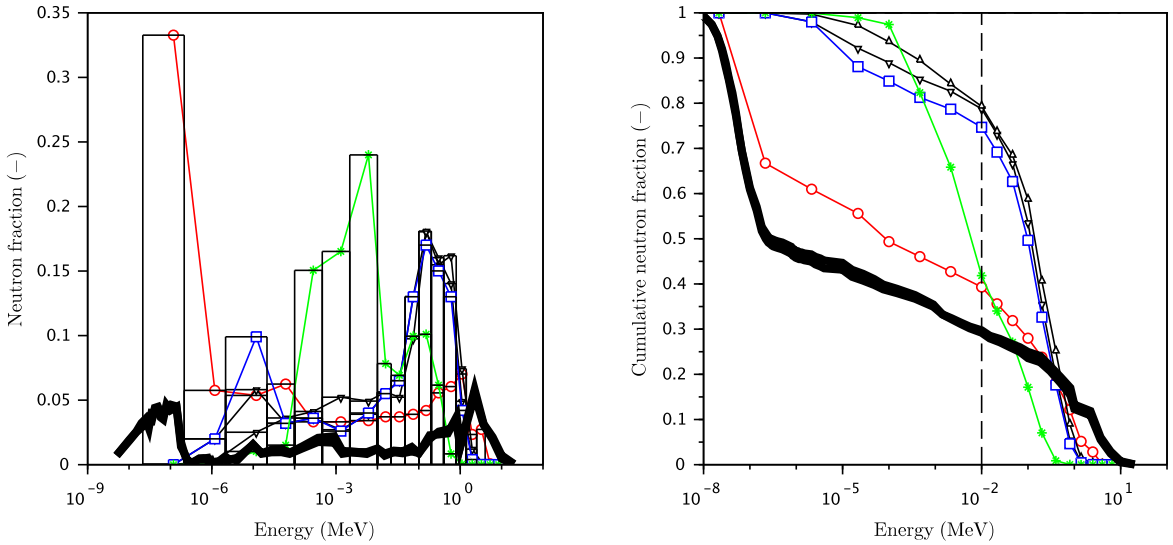

(Red) AM reactor, (black) OK50 and M1 channels in BR-5 reactor, (blue) OK70 channel in BR-10 reactor, (green) VEK channel in BOR-60 reactor, (thick black) cycle K224 in the XK1 position in LVR-15 reactor.

Figure 7. Neutron distribution per energy (Left) and cumulative neutron fraction (Right) .

Table 9. Relative contribution of fluence at energy higher than 10 keV to the total fluence in varied reactor positions.

reactor	position	ξ (-)
AM	02-13 and 07-06	0.392
BR-5	OK-50	0.787
	M-1	0.793
BR-10	OK-70	0.747
BOR-60	VEK	0.418
LVR-15	XK1	0.297

3.2 NEUTRON-INDUCED ATOM DISPLACEMENTS IN ROCK-FORMING MINERALS

This section includes excerpts from Remec et al. (2018) to clarify the methodology. The displacements per atom cross sections for neutrons for several common rock-forming minerals in concrete aggregates were generated using the SPECOMP computer code. This code is available as RSICC PSR-263, along with the SPECTER code and its database (Greenwood and Smither 1985; Greenwood 1988).

Selected minerals are quartz (SiO_2), calcite ($CaCO_3$, dimorphous form of aragonite), and feldspars: albite (sodium aluminum silicate, $NaAlSi_3O_8$), anorthite (calcium aluminum silicate, $CaAl_2Si_2O_8$), and microcline (potassium aluminum silicate, $KAlSi_3O_8$, dimorphous form of orthoclase), almandine ($Fe_3Al_2[SiO_4]_3$, from the garnet mineral group), and fayalite (Fe_2SiO_4, from the olivine mineral group). The atom displacement threshold energies (E_d) used were 31 eV for carbon, 30 eV for oxygen, 25 eV for sodium, 27 eV for aluminum, 25 eV for silicon, and 40 eV for potassium, calcium, and iron, which are the values that are usually used for these elements (Greenwood 1988). Using the same E_d for the elements in binary and more complex compounds is a common assumption because more detailed information is typically not available. The primary recoil atom energy distributions used were those available in the Specter database and were originally generated from ENDF/B-V neutron cross sections.

The dpa cross sections for all mineral exhibit very similar variations with energy: From a minimum at around 100 eV, the cross sections rapidly increase with increasing neutron energy. The increase is in part due to the increasing neutron energy and in part due to opening of additional reaction channels. The cross sections are about 3 orders of magnitude higher at 1 MeV than at 1 keV. At low neutron energies, the cross sections increase with decreasing energy, reflecting the typical $1/v$ increase in the neutron absorption cross sections (v is neutron velocity and is proportional to $E^{1/2}$).

The total displacement per atom rate is obtained as shown in Eq. (7):

$$\frac{\partial \text{dpa}}{\partial t} = \int_0^{+\infty} \sigma(E) \times \phi(E)\, dE, \tag{7}$$

where σ and ϕ are the energy-dependent cross section and the neutron flux, respectively. To evaluate the relative contributions of neutrons from different energies to the total dpa rate, the ratio of atom displacements that are induced by the neutrons with an energy above E_0 for a given neutron fluence rate spectrum reads

$$\frac{\frac{\partial \text{dpa}(E>E_0)}{\partial t}}{\frac{\partial \text{dpa}}{\partial t}} = \frac{\int_{E_0}^{+\infty} \sigma(E) \times \phi(E)\, dE}{\int_0^{+\infty} \sigma(E) \times \phi(E)\, dE} = \frac{\int_{E_0}^{+\infty} \sigma(E) \times \varpi(E)\, dE}{\int_0^{+\infty} \sigma(E) \times \varpi(E)\, dE}. \tag{8}$$

The Russian RIVE data are provided for fluence at energies higher than 10 keV. The fraction of total fluence at 10 keV reads

$$\frac{\Phi(E > 10\ \text{keV})}{\Phi(E > 0\ \text{keV})} = \int_{E>10\ \text{keV}}^{+\infty} \varpi(E) dE = \xi. \tag{9}$$

Hence, the total dpa is calculated by

$$\text{dpa} = \frac{\Phi(E > 10\ \text{keV})}{\xi} \underbrace{\int_0^{+\infty} \sigma(E) \times \varpi(E)\, dE}_{\delta}. \tag{10}$$

Table 10 provides the calculated values of ξ for varied reactor positions and rock-forming minerals. The corresponding dpa rates per neutron fluence (δ/ξ) are given in Table 11.

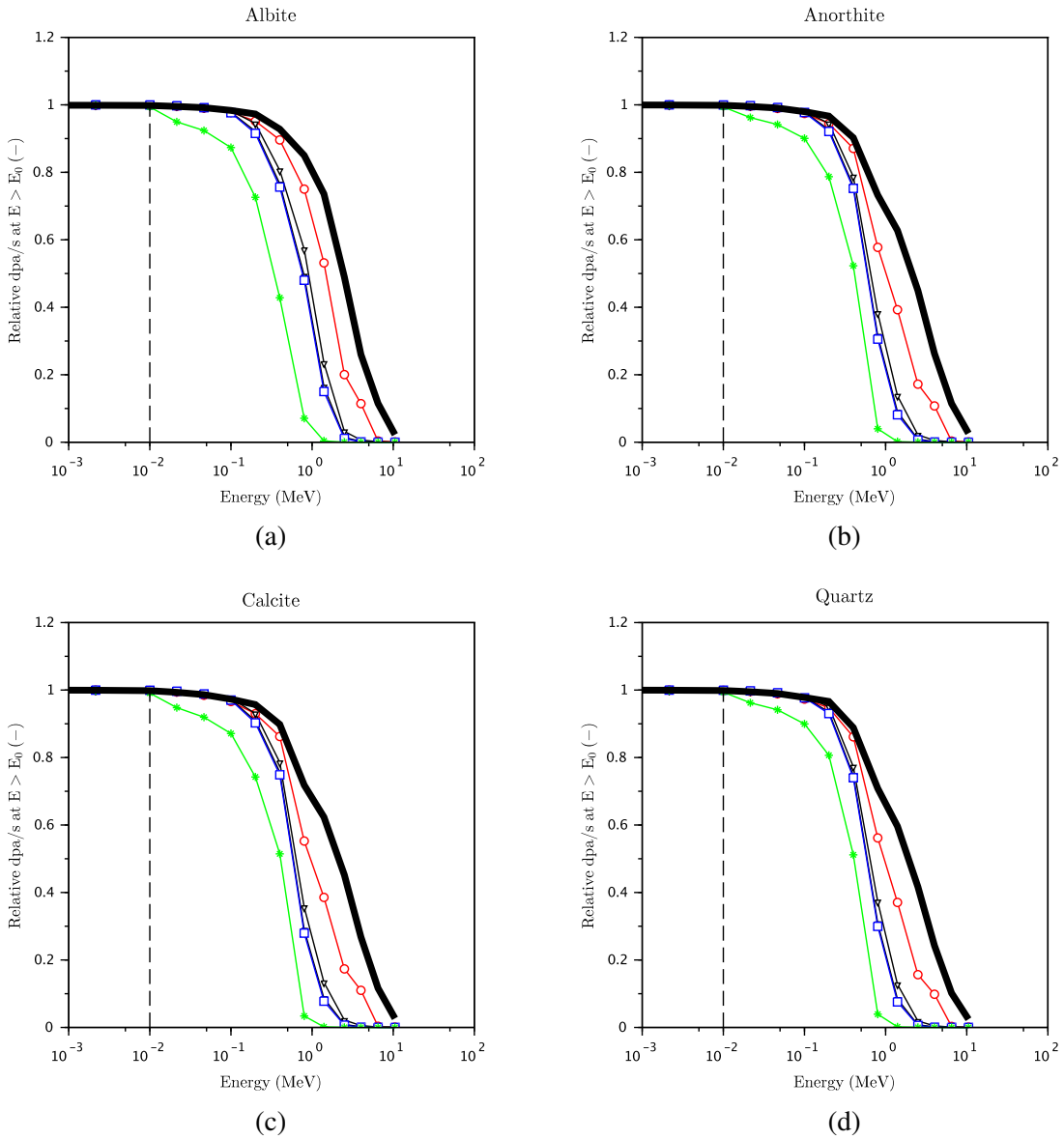

Figure 8. Cumulative dpa for energies $E > E_0$ for (a) albite, (b) anorthite, (c) calcite and (d) quartz. Same color legend as in previous figure.

For quartz, δ/ξ is close to 0.1 dpa per n·pm^{-2} but for the VEK position in the BOR-60 reactor ($\delta/\xi \approx 0.07$ dpa per n·cm^{-2}. Thus, the scatter plots showing quartz RIVE as functions of the fast neutron fluence in Figure 9 (Left) and the dpas in Figure 9 (Center) remain quite similar. The values of δ/ξ for anorthite and calcite in all reactors but the BOR-60 are also comparable. The values of δ/ξ for albite are more dispersed, ranging between $\approx$ 0.03 dpa per n·pm^{-2} to $\approx$ 0.1 dpa per n·pm^{-2}. This study needs to be refined to include other common rock-forming minerals. However, considering that quartz is the main contributor to aggregate RIVE, it appears that expressing RIVE as a function of dpa instead of fast neutron fluence at energies higher than 10 keV does not significantly affect the representation of RIVE data collected in the IMAC database.

Table 10. Cumulative dpa rates for varied rock-forming minerals and reactor positions.

		$\delta \times 10^{-24}$ per n·cm^{-2}			
reactor	position	quartz	albite	anorthite	calcite
AM	02-13 and 07-06	394.0	318.3	367.9	303.0
BR-5	OK-50	776.6	490.6	700.0	578.8
	M-1	822.2	551.9	742.5	608.6
BR-10	OK-70	723.5	453.4	651.9	539.9
BOR-60	VEK	277.1	143.9	247.5	216.5
LVR-15	XK1	299.2	329.2	318.8	262.2

Table 11. dpa rates per neutron fluence for varied rock-forming minerals and reactor positions.

		$\delta/\xi \times 10^{-20}$ per n·cm^{-2}			
reactor	position	quartz	albite	anorthite	calcite
AM	02-13 and 07-06	0.1005	0.0812	0.0938	0.0773
BR-5	OK-50	0.0986	0.0623	0.0889	0.0735
	M-1	0.1036	0.0696	0.0939	0.0769
BR-10	OK-70	0.0968	0.0607	0.0873	0.0723
BOR-60	VEK	0.0662	0.0344	0.0592	0.0517
LVR-15	XK1	0.1007	0.1084	0.1073	0.0883

3.3 RUSSIAN DATA

Assuming that the fast neutron flux is constant, the apparent dpa (noted here dpa_{app}) can be approximated by:

$$\text{dpa}_{\text{app}} = \dot{\Phi} t \frac{\delta}{\xi} \tag{11}$$

A first interpretation of Denisov's data was developed in Le Pape, Alsaid, and Giorla (2018) to provide empirical relations estimating rock-forming minerals' RIVE as a function of the fast neutron fluence and average irradiation temperature: $\varepsilon^*(\Phi, T)$. This expression can also be interpreted as $\varepsilon^*(\xi \text{dpa}_{\text{app}}/\delta, T)$. It can be observed in Figure 9 and Table 11 that replotting the RIVE data using dpa_{app} instead of Φ leads to comparable trends because the values of δ/ξ are generally around 0.1×10^{24} per n·cm^{-2}. Using XRD analysis, Bykov et al. (1981) noted that the lattice changes were comparable for a given RIVE value independently of the irradiation conditions. Therefore, it can be assumed that the effective dpa is unambiguous for a given RIVE value. Assuming that at low irradiation temperatures around 25 °C annealing effects are not significant, the effective dpa can be approximated as $\text{dpa}_{\text{eff}} \sim \text{dpa}_{\text{app}}(T \sim 25\ ^{\text{o}}\text{C})$. Each post-irradiation RIVE data point can be interpreted using the equation $\varepsilon^*(\text{dpa}_{\text{app}}, T) \sim \varepsilon^*(\text{dpa}_{\text{eff}}, T \sim 25\ ^{\text{o}}\text{C})$ to plot the ratio $\text{dpa}_{\text{app}}/\text{dpa}_{\text{eff}}$ as a function of the irradiation temperature in Figure 10 (Left). Except for the data corresponding to irradiation

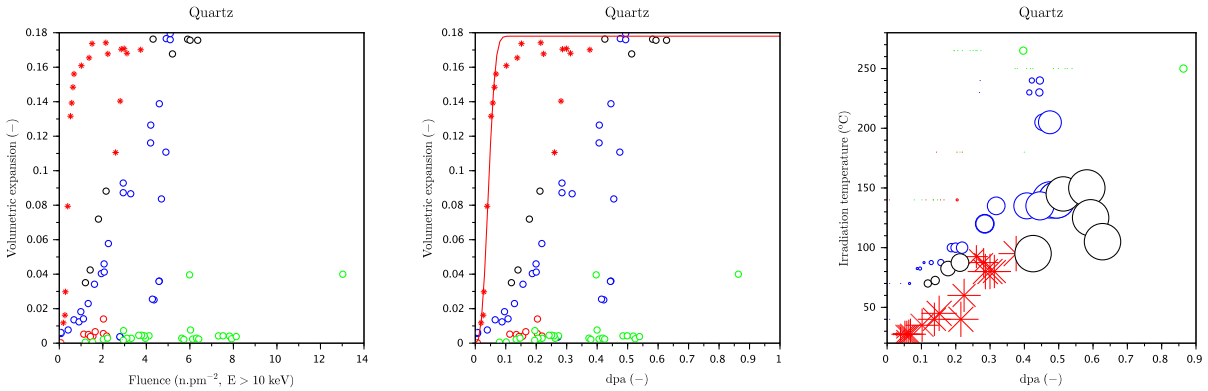

(Left) RIVE as a function of the fast neutron fluence; (Center) RIVE as a function of the dpa; and (Left) RIVE as a function of dpa and average irradiation temperature. Red marks: channels 02-13 and 07-06 of the AM reactor, Black marks: channels OK-50 and M-1 of the BR-5 reactor, Blue marks: channel OK-70 of the BR-10 reactor, and Green marks: VEK channel of the BOR-60 reactor.

Figure 9. RIVE data (Bykov et al. 1981; Denisov, Dubrovskii, and Solovyov 2012) .

experiments conducted in the VEK channel of the BOR-60 reactor, $\text{dpa}_{\text{app}}/\text{dpa}_{\text{eff}}$ appears to follow some linear trend with the irradiation temperature. It can also be observed that the ratio $\text{dpa}_{\text{app}}/\text{dpa}_{\text{eff}}$ is already ≈ 5 at 100 °C, which implies that about 80% of the defects are annealed. Another representation of the effects of annealing is provided in Figure 10 (Right) assuming the expression$\text{dpa}_{\text{eff}} \sim \text{dpa}_{\text{app}} \exp\left[-\tau(1/T_{ref} - 1/T)\right]$, where dpa_{app} and dpa_{eff} represent the apparent displacement per atom determined from the fast neutron dose and reactor spectrum, and the *effective displacement per atom*, respectively. The concept of *effective dpa* is introduced here to account for RIVE at a low reference temperature $T - ref \approx 30$ °C, where annealing effects are considered negligible. Best fitting analysis leads to $\tau \approx 1009$ K.

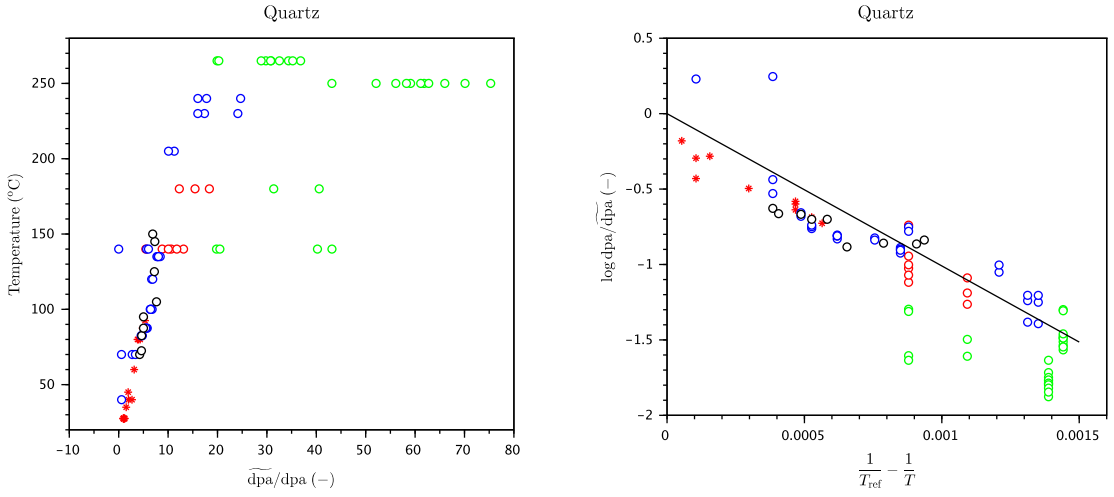

Figure 10. Relation between the irradiation temperature and the ratio $\text{dpa}_{\text{app}}/\text{dpa}_{\text{eff}}$ (Left); thermal annealing activation (Right). Color marks identical to Figure 9.

In conclusion, expressing the RIVE as a function of displacements per atom, rather than fast neutron fluence, offers a comparable representation of the RIVE of quartz at various irradiation temperatures. However, the

effects of irradiation temperature remain predominant in influencing the RIVE rate. The observed mechanisms of annealing during neutron irradiation require further study.

4. RADIATION-INDUCED DAMAGE AND ANNEALING

4.1 NATURE OF DEFECTS IN ROCK-FORMING MINERALS

Molecular dynamics (MD) simulations of irradiation-induced defects in α-quartz show that the ends of the cascades mainly consist of over-coordinated Si and O atoms, as well as Si−O connectivity defect, such as small Si−O rings and edge-sharing Si tetrahedra (Wang et al. 2015) (Figure 11). Annealing of oxygen vacancies caused by cascades occurs primarily by local relaxation around the vacancies (Wang et al. 2015).

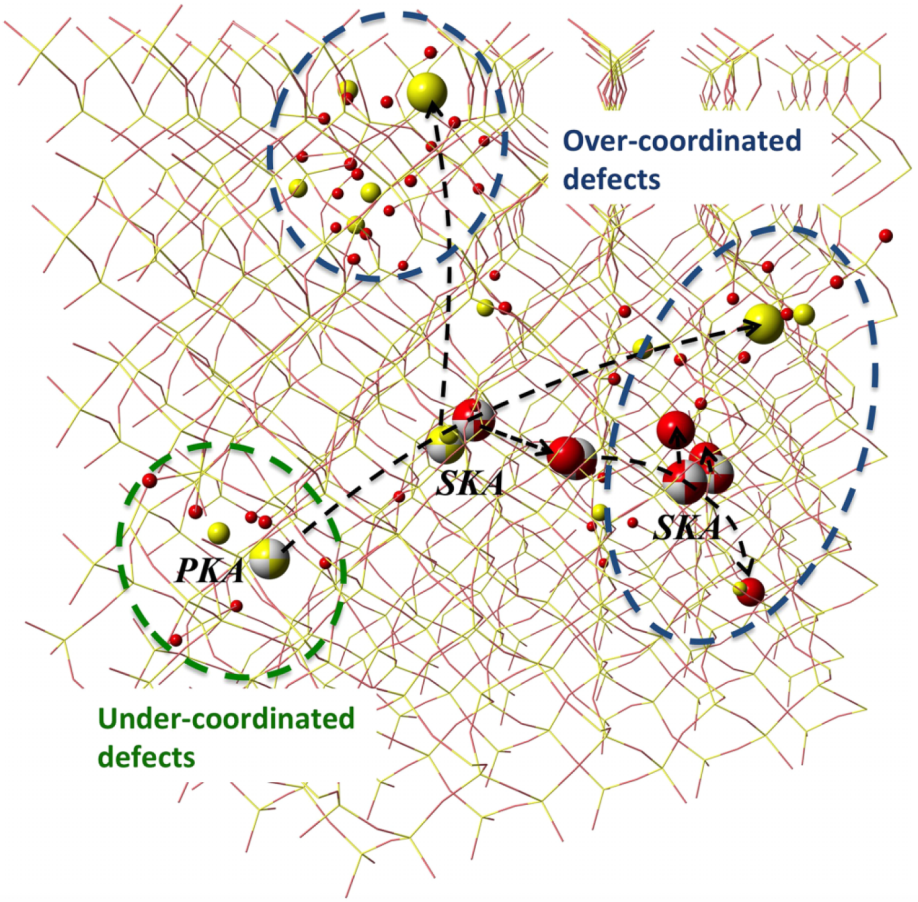

Figure 11. Example of a 600 eV cascade trajectory in α-quartz. Silicon and oxygen atoms with displacements greater than 1 Å are shown as yellow and red spheres, respectively. Major high-velocity atoms during the cascade, such as the primary knock-on atom (PKA) and secondary knock-on atom (SKA) are highlighted with exaggerated sizes, and their initial positions are shown with beach balls. Reproduced from (Wang et al. 2015). **Reproduction rights to be requested (American Institute of Physics, Journal of Chemical Physics).**

Rock-forming minerals have ionic and covalent bonds. In silicates, the ratio of covalent to ionic bonds increases with the degree of polymerization of the SiO_4^{4-} tetrahedra. Tectosilicates (quartz, feldspars) are less *ionic* than phyllosilicates, followed by inosilicates and orthosilicates. α-quartz crystals contain only covalent bonds. Irradiation-induced physical properties of silicates are greatly affected by the cross-linking of SiO_4^{4-} (Le Pape, Alsaid, and Giorla 2018). For the sake of illustrating this effect, consider the following. Ion-irradiation-induced metamictization of rock-forming silicates increases their dissolution rates in contact with

alkaline solution (Ichikawa and Miura 2007; Pignatelli et al. 2016; Hsiao et al. 2017; Hsiao et al. 2018). An increase in dissolution rate correlates with irradiation-induced density change: quartz (density change ~15%, dissolution rate ×100), albite (Na-bearing feldspar, density change ~7%, dissolution rate ×15), almandine (Fe−Al garnet, density change: 1%, dissolution rate: × ~ 2).

Irradiation-induced defects, such as vacancies and interstitials, can move if the temperature is sufficiently high, which can alter the irradiation damage and potentially lead to complete healing. This annealing effect occurs in all materials, even at relatively low temperatures. The mobility of defects differs between ionic and covalent systems (e.g., semiconductors). "In ionic crystals, both self-diffusion and conduction of electricity (above room temperature) proceed by the motion of lattice vacancies. In general the variation in mobility from one ion to another depends primarily on the sizes of the ions, smaller ions being more mobile as interstitials" (Dienes and Vineyard 1957). Calculated activation energies (E_m) in alkali halides (e.g., NaCl) appear to range between 0.4 and 1.2 eV. The mobility of defects is proportional to $T^{-1}\exp(-E_m/kT)$.

Because Bykov et al. (1981) observed that the irradiation temperature in the range of ≈ 30 °C to ≈ 300 °C significantly affects the RIVE rate—the higher the irradiation temperature, the lower the rate—it can be hypothesized that this effect is governed by thermal annealing. In this section, we examine published results from post-irradiation annealing experiments (Primak 1958; Yano et al. 2007) and interpret these data using a simple activation energy spectrum model proposed by Hickman and Pryor (1964). This model is then applied to neutron irradiation experiments conducted at various temperatures to study the effects of thermal annealing on the RIVE rate.

4.2 ANNEALING EXPERIMENTS

4.3 POST-IRRADIATION ANNEALING

Post-irradiation thermal experiments (annealing) on quartz and vitreous silica were conducted by Mayer and Lecomte (1960), Primak (1958), and Yano et al. (2007). The latter illustrates the evolution of post-irradiation expansion in quartz during isochronal thermal heating up to approximately 1,000 °C at a rate of about 1,000 °C h^{-1} (Yano et al. 2007). For specimens irradiated at low fluence, annealing, or "self-healing"—where the material evolves toward α-quartz—is observed, accompanied by a reduction in expansion to the initial quartz density value. Conversely, after irradiation at high fluence, anti-annealing is observed: quartz evolves toward more amorphous forms, referred to as *cryptocrystalline* by Wittels (1957), although these forms differ from vitreous silica unless a fluence on the order of 10^{20} n·cm^{-2} is reached (Primak 1958). Mayer and Lecomte (1960) estimated the dose threshold separating annealing from anti-annealing behavior at approximately 0.65×10^{19} n·cm^{-2} for energies above 0.3 MeV (Keppens and Laermans 1996).

4.3.1 Interpretation Model

Primak (1958) observed that quartz "anneals simply over a broad range of temperatures, suggesting a broad activation-energy spectrum for annealing of the disorder." Thus, the proposed rate model is not limited to a single activation energy. To analyze post–neutron irradiation annealing data for beryllium oxide, Hickman and Pryor (1964) proposed such an activation energy spectrum model. During irradiation, defects are produced at a rate of $K\dot{\Phi}$, where $\dot{\Phi}$ is the neutron flux. This defect production is comparable to that described by Eq. (11). However, Hickman uses the concept of defects in a broader sense than the displacements per atom metric. Annealing effects during irradiation are assumed to occur with a spectrum of activation energies ranging from Q_1 to Q_2 following first-order kinetics. By integrating the solution for a single activation energy over the range $Q1 \rightarrow 2$), the defect concentration during irradiation is expressed as follows:

$$N = K\dot{\Phi}t\frac{kT}{Q_2 - Q_1}\left[\beta(A_2 t) - \beta(A_2 t)\right]. \tag{12}$$

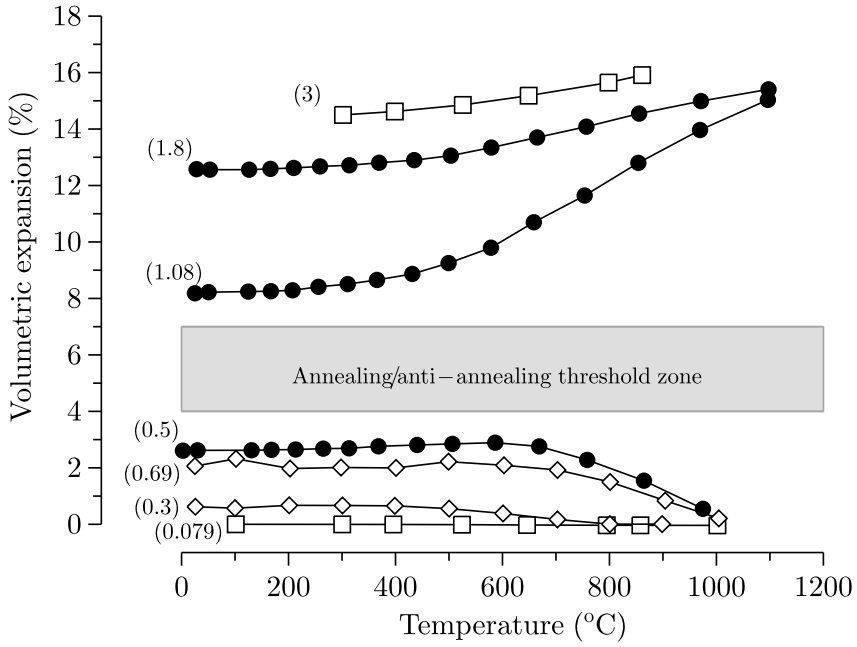

Figure 12. Post-irradiation annealing or anti-annealing of quartz. The fluence level before thermal treatment is given in brackets $\times 10^{20}$ n·cm^{-2}. •: from dimensional change measurements (Primak 1958); □: from density measurements (Primak 1958); ⋄: from dimensional change measurements (Yano et al. 2007).

In this equation, k represents the Boltzmann constant ($k = 1.380649 \times 10^{-23}$ J K^{-1}). T is the irradiation temperature assumed constant during the experiment. $\beta(z) = (1 - e^{-z})/z + \mathrm{Ei}(z)$, where Ei is the exponential integral function. (Note that $Ei(-z) = -\mathrm{Ei}(z) = \int_{-\infty}^{-z} \exp(x)/x \; dx$.) A_1 and A_2 are derived from the expression$A_i = A_0 \exp(-Q_i/kT)$. The A_i term has the dimension of a time inverse. When N represents $\mathrm{dpa}_{\mathrm{eff}}$, Eq. (12) can be rewritten in the compact form $\mathrm{dpa}_{\mathrm{eff}} = \mathrm{dpa}_{\mathrm{app}} \, \mathcal{F}(T, t)$. The effective defect production depends on both temperature and time, whereas the model used for interpreting Denisov's data accounted only for temperature effects. This model can also be applied to interpret annealing experiments. The ratio of remaining defects N to the post-irradiation defects N_0 is given by

$$\frac{N}{N_0} = \frac{kT}{Q_2 - Q_1} \left[\mathrm{Ei}(A_2 t_a) - \mathrm{Ei}(A_1 t_a) \right], \tag{13}$$

where t_a and T are the annealing time and temperature. Equation (13) is governed by three parameters: the annealing rate constant A_0 and the annealing energy range values Q_1 and Q_2. To analyze annealing experiments on neutron-irradiated BeO, Hickman and Pryor (1964) proposed setting the value of A_0 to 3×10^{10} s^{-1}; they then calibrated values of 1.3 eV and 3.9 eV for Q_1 and Q_2, respectively, to achieve a good fit of the theory to the available data. The value of A_0 was "chosen corresponding to diffusion over a few hundred Angstroms (Dienes and Vineyard 1957)".

4.3.2 Post JMTR Irradiation Annealing of Pure Quartz

Yano et al. (2007) measured the dimensional change and lattice change parameters of high-purity single-crystal α-quartz (SEIKO Denshi. Ltd.) after neutron irradiation conducted in the Japan Materials Testing Reactor (JMTR) up to a fluence of 3.0×10^{19} n·cm^{-2} ($E > 0.1$ MeV) at 140 °C, and 6.9×10^{19} n·cm^{-2} at

300 °C. The average length change of the irradiated quartz along the c-axis was 0.09(0.01)% and 0.17(0.13)% for fluences of 3.0×10^{19} n·cm^{-2} and 6.9×10^{19} n·cm^{-2}, respectively, whereas changes along the a-axis were 0.31(0.11)% and 0.99(0.60)%, respectively. The a/c ratios were 3.44 at 3.0×10^{19} n·cm^{-2} and 5.82 at 6.9×10^{19} n·cm^{-2}. The volumetric changes can be estimated from the lattice changes using the assumption $\Delta v/v0 \sim 2\Delta a/a_0 + \Delta c/c_0$) (Primak 1958), resulting in 0.71% and 2.15% for the two fluence levels, respectively. However, the volumetric changes derived from density measurements are 2.35% and 2.05% for fluences of 3.0×10^{19} and 6.9×10^{19} n·cm^{-2}, respectively. These values do not agree with the work of Bykov et al. (1981), which suggests that at the fluences and irradiation temperatures tested in the JMTR, the volumetric expansion of quartz is unlikely to exceed 1%. Using the empirical model derived from Bykov's data (Le Pape, Alsaid, and Giorla 2018), the estimated volumetric expansions are 0.19% and 0.01%. The discrepancy may be attributed to a lack of detailed information about the irradiation conditions in the JMTR.

Nevertheless, the value of the Yano et al. (2007) data lies in the post–neutron irradiation annealing experiments conducted isochronally for 1 h in vacuum, with temperatures ranging from 100 °C to 1000 °C. The annealing data (lattice cell parameters and dimensional changes) were normalized to their respective post-irradiation measurements and are plotted in Figure 13. Measurements corresponding to the a and c crystalline directions are represented by circles and squares, respectively. With the exception of the dimensional measurements along the c direction, the data are consistent and were used to calibrate the model described by Eq. (13). This assumes that the relative dimensions are representative of defect evolution: that is, $l/l_0 \sim N/N_0$.

As a preliminary attempt, the value of A_0 was assumed to be 3×10^{10} s^{-1} (Hickman and Pryor 1964). The values of Q_1 and Q_2 were calibrated to match the observed trend finding $Q_1 = 2$ eV and $Q_1 = 10$ eV. It must be acknowledged that the determination of the triplet (A_0, Q_1, Q_2) is ambiguous and depends on the first assumption made about the value of A_0. The figure also shows the calibrated annealing curve obtained when assuming $A_0 = 3 \times 10^9$ s^{-1}, which provides another reasonable fit to the data. It is noteworthy that both sets of fitting parameters lead to annealing occurring at temperatures above 600 °C, which aligns with Yano's observation that annealing began around 500 °C and was completed around 800 °C. With the given fitting parameters, the defect formation during irradiation described by Eq. (12) is minimally affected at in-service temperatures in LWRs, regardless of the fast neutron flux. A similar observation was made regarding the annealing effects during irradiation reported by Bykov et al. (1981)–see Figure 9 (Right). (*i*) Dimensional changes (length and lattice parameters) may not be representative of defect production, or (*ii*) The annealing mechanisms occurring during irradiation may differ from those observed in post-irradiation annealing experiments.

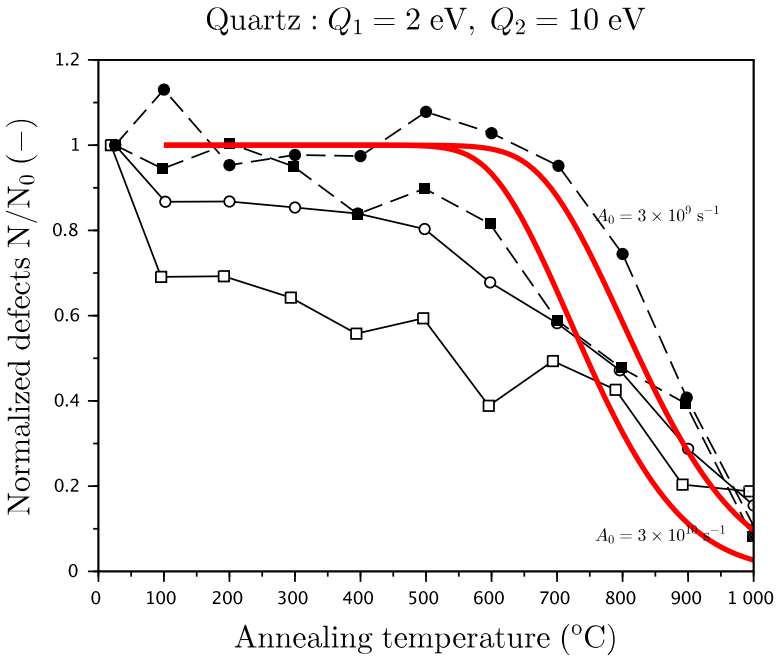

Figure 13. Relative lengths (black marks) and lattice (empty marks) parameters during continuous annealing. Modeled annealing from Eq. (13).

4.3.3 Post Hanford–LITR–MTR Irradiation Annealing of Natural Quartz

Primak (1958) reported annealing data obtained on natural quartz specimens that were previously irradiated in three reactors: the Hanford reactor (presumably the water-cooled 250 MW B reactor, with an irradiation temperature below 60 °C), the Low Intensity Test Reactor (LITR) at ORNL (specimens in contact with unforced circulation coolant water at approximately 50 °C), and the 40 MW Materials Testing Reactor (MTR) (specimens in contact with forced circulation coolant water at approximately 40 °C) at ORNL.

From the post-irradiation analysis, the specimens have been categorized into loosely defined stages: (I) *early* stage ($\Phi < 5 \times 10^{19}$ n·cm^{-2}), (II) *late* stage, and (III) *final late* stage ($\Phi > 11 \times 10^{19}$ n·cm^{-2} – cutoff energy not provided). In addition, 'A' and 'B' refer to the initial and later portion of each stage. All of the annealing experiments reported by Primak (1958) were conducted in a step-by-step manner. The specimen was heated to the desired temperature for a duration on the order of 10^3 s (with 30 minutes also reported in the same article). The specimen was then cooled, measured, and the heating process was repeated at a higher temperature. During various annealing steps, measurements were taken for density, length changes along the *c* axis and perpendicular to it, refractive index, and rotary power.

Figure 14 shows the density and length changes reported in Primak (1958) for stages I (left), II (center), and III (right). Black, red, and blue marks correspond to density, length perpendicular to the *c* axis, and length parallel to the *c* axis, respectively. The data are normalized to the corresponding values after irradiation. It can be observed that for specimens irradiated in the early stage, increasing temperatures lead to annealing, characterized by a reduction in dimensional changes and density. In contrast, for specimens in the late stages, dimensions continue to increase, a phenomenon referred to as *anti-annealing*. The specific damage domain responsible for the transition between annealing and anti-annealing is not clearly defined. A rough boundary between the early and late stages appears to be around 5×10^{19} n·cm^{-2} at $T \sim 45$ °C. The proposed annealing model appears to be applicable only to the early stage data.

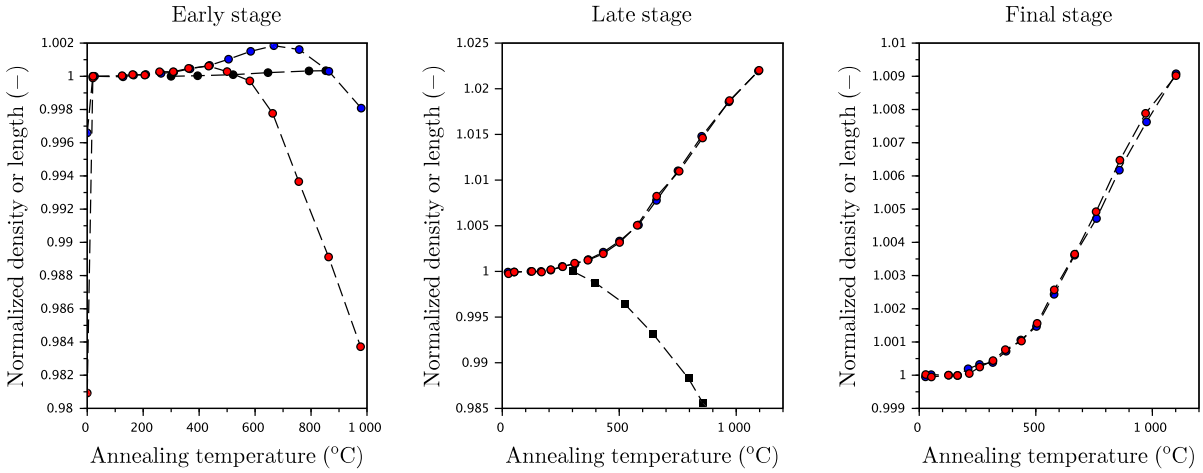

Figure 14. Density and length change during annealing of quartz specimens irradiated at varied neutron doses. (Black): density, (red): parallel to the c axis, (blue): perpendicular to the c axis.

The volumetric change can be calculated from the density change ($\Delta v/v_0 = (\Delta\rho/\rho_0)/(1 + \Delta\rho/\rho_0)$) or the dimensional changes ($\Delta v/v_0 = 2\Delta a/a_0 + \Delta c/c_0$), where a is the length perpendicular to the c-axis. Circle and square marks correspond to the density-derived (specimen 671) and length-derived (specimen 760/761) volumetric changes. The estimated neutron doses for specimens 671 and 760/761 are 0.79×10^{19} n·cm^{-2} and 5×10^{19} n·cm^{-2}. The corresponding percentages of irradiation-induced volumetric change are 0.61% and $\sim$ 4.25%. Annealing causes a decrease of volume for specimen 760/761 that is almost complete at 1100 °C. However, specimen 671 does not show any volume change. Only specimen 760/761 was used to calibrate the annealing model described by Eq. (13).

Using the empirical models derived from the interpretation of the Bykov et al. (1981) data, and assuming that the fluence provided by Primak is close to the fluence at $E > 10$ keV, the irradiation-induced volumetric changes are in the range of 0.44%–0.62% and 4.8%–6.8% at irradiation temperatures of 40 °C and 50 °C, respectively, for specimens 671 and 760/761. These estimated values are similar to those of the post-irradiation measurements. Thus, the volumetric change during annealing can also be analyzed to find the equivalent fluence that would have caused that volumetric change at the same irradiation temperature. Because dpa $\propto \Phi$, this equivalent fluence can be considered as an approximate measure of the corresponding irradiation damage. Figure 16 shows the evolution of the annealing-induced volumetric change with the equivalent fluence. The trend is somewhat linear with a loss of linearity toward the final stage of the annealing experiment. This observation makes it possible to assume that the volumetric change during annealing is a reasonable estimate of damage-induced defects.

The annealing model—Eq. (13)—was first tested using the set parameters derived from the analysis of Yano's data (red cures in Figure 17). Using those parameters results in an underestimation of the onset of annealing. However, the model is quite sensitive to rather small changes in the governing parameters. The blue curve was obtained using the following set: $A_0 = 3 \times 10^{10}$ s^{-1}, $Q_1 = 2.45$ eV, and $Q_2 = 10$ eV.

Using the obtained set of parameters, the effects of irradiation duration and temperature can be estimated from Eq. (12). The result of such a parametric study is provided in Figure 18. It can be observed that for temperatures < 350 °C, there is no significant effect on the defects production independently of the irradiation duration (< 80 years). This theoretical observation contradicts the extensive data on irradiated quartz expansion reported by Bykov et al. (1981)—see Figure 6. This suggests that thermal annealing is unlikely to be a dominant mechanism for defect healing during neutron irradiation at temperatures $\lessapprox 350$ °C.

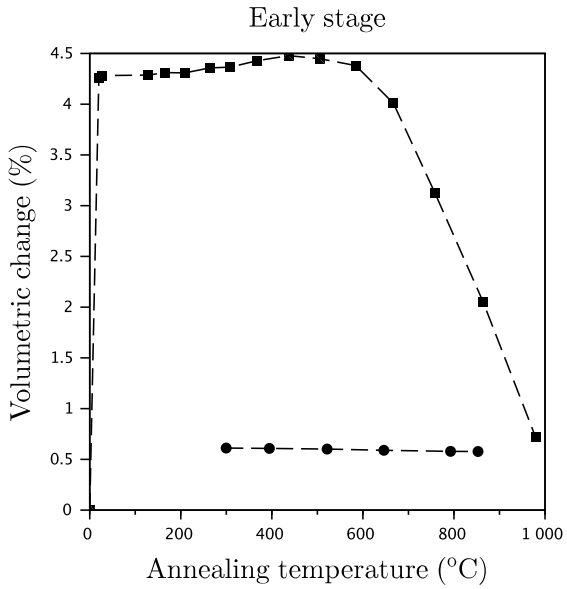

Figure 15. Volumetric change caused by irradiation (early stage) and post-irradiation annealing—Primak (1958) data.

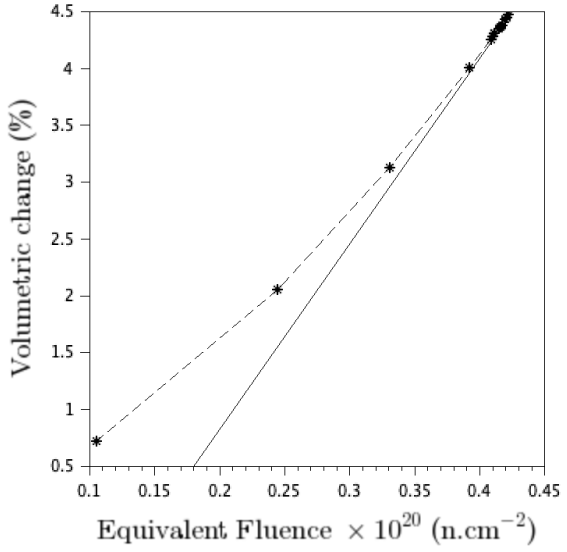

Figure 16. Interpretation of volumetric change during post-irradiation annealing experiment with equivalent fluence.

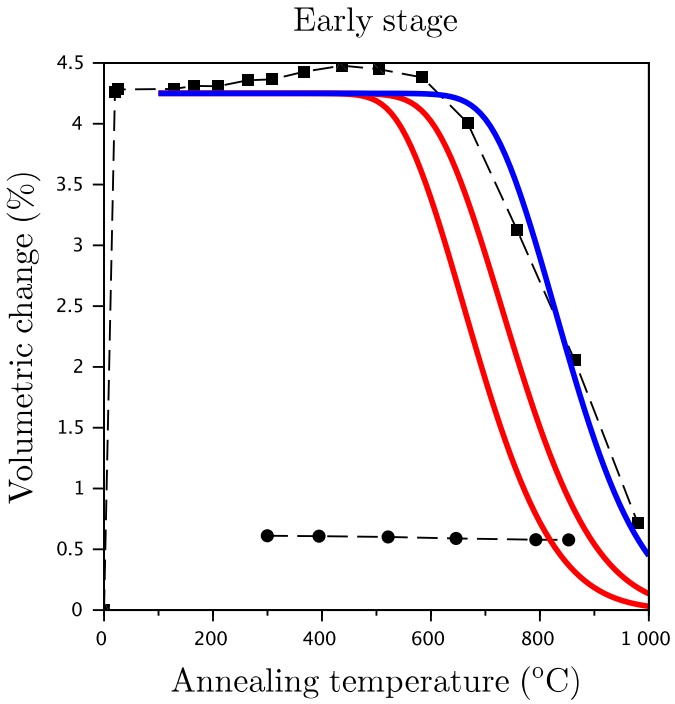

Figure 17. Annealing model fitted on specimen 760/761 data. $A_0 = 3 \times 10^{10}$ s^{-1}, $Q_1 = 2.45$ eV, and $Q_2 = 10$ eV.

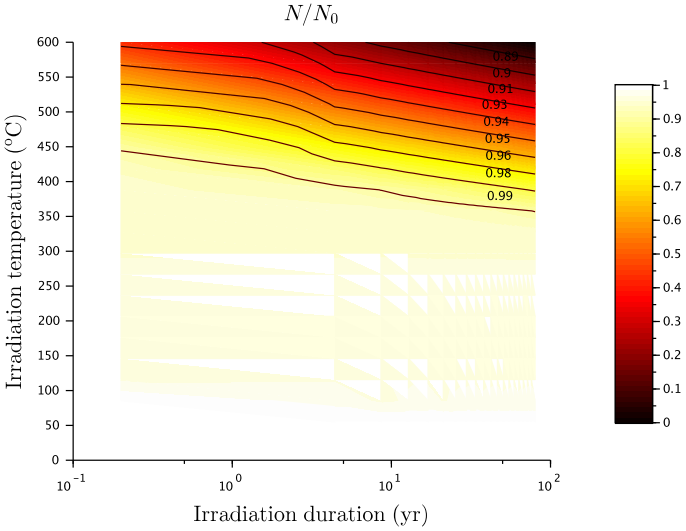

Figure 18. Defects production during irradiation at varied temperature and duration. Obtained from Eq. (12) using the parameters fitted on Primak's data.

5. IONIZATION-ENHANCED ANNEALING

As shown in the previous section, thermal annealing is unlikely to cause the observed effects during neutron irradiation. Therefore, the apparent temperature dependence of the RIVE rate observed by Bykov et al. (1981) and Denisov, Dubrovskii, and Solovyov (2012) needs to be re-evaluated considering that irradiation temperature is indicative of energy deposition–induced heating caused by neutrons and gamma-rays. Irradiation interaction with matter includes nuclear (ballistic effect) and electronic energy (ionization) loss effects. Ionizing radiation is caused by subatomic particles and electromagnetic waves (electron, gamma, x-ray). When interacting with atoms, they result in detaching electrons. The interactions between nuclear stoppage–induced defects and electronic stoppage–induced defects in rock-forming minerals require evaluation. This subject is complex, and only a preliminary literature review of the effect of ionizing radiation on quartz and silica was conducted during fiscal year 2024.

Electron Irradiation

"That radiation damage and eventual *metamictization* in α-quartz has been shown to arise from the ionizing component of radiation means that an intrinsic *radiolytic* mechanism must be responsible" (Hobbs and Pascucci 1980).

A similar conclusion was drawn by Pfeffer 1985 on SiO_2 irradiated under 30-160 keV beam: "ionization rather than atomic displacement is the predominant formation mechanism. Significant differences in dose dependence were found between oxide types, reflecting the role of hydrogen in damage annealing."

Hobbs and Pascucci (1980) proposed a three-stage model for 20–125 keV electron irradiation-induced metamictization (amorphization):

1. First, early formation of strained amorphized inclusions are created at heterogeneous nucleation sites (electron dose of $\sim$ 10 GGy, i.e., $\sim 6 \times 10^{25}$ eV g^{-1}). The defect mobility appears to be high, causing the propagation of nucleated defects outside the amorphized regions.

2. Second, ionization radiation–induced localized excitation in SiO_2 systems can damage the Si−O bond (energy $\sim$ 5 eV – see Figure 19(a)). Subsequently, the bridging oxygen is removed to form a neutral oxygen vacancy E" center ($\equiv$Si−Si$\equiv$ $\longrightarrow$ $\equiv$Si$^{\cdot}$ $^{+}$Si$\equiv$) stabilized by a Si−Si bond. The removed oxygen is incorporated into an Si−O−O−Si peroxy linkage involving a neighboring Si−O bond. The oxygen vacancy and peroxy linkage form the components of a closely spaced Frenkel pair—see Figure 19(b).

3. Finally, the reorganization (tetrahedron reorientation and re-bonding) toward a less dense structure occurs when the local density of oxygen vacancies become sufficiently high. This stage is completed at an electron dose of $\sim$ 10 TGy, that is, $\sim 6 \times 10^{27}$ eV g^{-1}.

Significant differences in dose dependence have been observed by Pfeffer (1985) between oxide types, reflecting the role of hydrogen in damage annealing.

Muto and Maruyama (2016) found that rock-forming minerals specimens exposed to a 100 keV electron beam were amorphized at doses of 10^{21}, 2.5×10^{21}, and 2.5×10^{22} e·cm^2 for α-quartz, orthoclase, and muscovite, respectively. The corresponding density changes seems to evolve toward plateaus at the highest doses to reach values of 4%, 1.3%, and 5.5% respectively. Those values are much lower than the maximum density changes observed on specimens irradiated by neutrons (Wittels 1957; Primak 1958; Denisov, Dubrovskii, and Solovyov 2012). Such an observation was previously made from other post-irradiation examination of ceramics: "The volumetric swelling in Al_2O_3 and MgO was found to be much lower in specimens irradiated at room temperature with light ions such as H+ than in specimens irradiated with heavier ions to the same

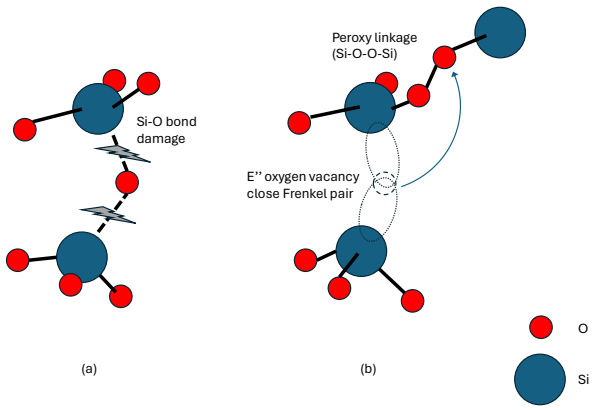

Figure 19. Hobbs and Pascucci's radiolysis model. a) Instability of excited Si−O bond(s) leads to bond-breakage and b) formation of −O−O− peroxy linkage and E" oxygen vacancy close Frenkel pair. (Adapted from the original figure).

calculated damage level (Krefft 1977; Krefft and EerNisse 1978). In addition, studies have shown that the volume expansion in Al_2O_3, BeO, or MgO induced by heavy ion or fission neutron irradiation may be recovered by subsequent electron or H^+ ion irradiation (Krefft 1977; Krefft and EerNisse 1978; Walker 1964)" (Zinkle 1995).

Gamma Irradiation

Imai et al. (1993) conducted gamma irradiation (Co^{60} source, 10 kGy h^{-1}, maximum dose <~ 10 MGy) at room temperature and 77 K on synthetic silica containing varied F, OH, Cl impurities. The concentration of oxygen vacancies and non-bridging oxygen hole centers evolves approximately as a square root of the gamma dose, independently of the pre-existing defects concentration. The damage mechanism is similar to the electron-induced damage formation observed by Hobbs and Pascucci (1980): First, it forms strain bond cleavage ($\equiv Si-O-Si\equiv \longrightarrow Si^{\cdot}\ {}^{\cdot}O-Si\equiv$), and, second, E' centers react with interstitially existing molecular oxygen to form peroxy radicals ($\equiv Si^{\cdot} + O_2 \longrightarrow \equiv Si-O-O^{\cdot}$). The growth of E' centers at room temperature seems comparable irrespective of the irradiation source (γ, x-ray, and laser) at equivalent absorbed energy levels.

Preliminary Hypothesis

This brief review of the effect of electron and gamma irradiation of quartz and silica indicates that the ionization-induced damage is governed by short-range defects production. The ballistic interactions between fast neutrons and quartz cause longer-range structural defects, including bond breakage and crystalline network distortion—for example, as suggested in Wang et al. (2015).

The synergistic effects between short- and long-range defects in rock-forming minerals need to be investigated because there is evidence of subsequent ionization-induced annealing of pre-existing damage in ionic compounds caused by heavy ions irradiation.

6. CONCLUSIONS

In the first part of this report, MOSAIC 3D simulations are presented, illustrating the effects of irradiation on representative synthetic concrete microstructures. The microstructures correspond to well-characterized concretes: Con-A, which contains a metachert rich in quartz, and Con-B, which is composed of sandstone. The XRD-based chemical composition of the aggregates is accounted for in the microstructures. Both pristine and irradiated specimens of these concretes have been thoroughly characterized by JCAMP and ORNL after irradiation in the now-decommissioned JEEP-II reactor and the LVR-15 reactor. The simulated neutron radiation–induced dimensional changes for both concretes irradiated in the JEEP-II reactor were found to be in agreement with post-irradiation measurements. Additionally, the simulations align well with analytical solutions that account for the total volume fraction of aggregates and the combined contribution of each aggregate-forming mineral's RIVE, weighted by their respective volume fractions. Although the RIVE values obtained from analytical and 3D MOSAIC simulation results are comparable, both approaches overestimated the dimensional changes in concrete specimens Con-A and Con-B irradiated in the out-of-core XK1 position of the LVR-15 reactor, where the fast neutron flux was 10 times lower than in the JEEP-II reactor. This observation, combined with additional data from the JCAMP team on aggregates irradiated in different positions within the LVR-15 reactor, suggests that the fast neutron flux significantly affects the RIVE rate. Noting that the fast neutron flux during in-service irradiation in LWRs is one to two orders of magnitude lower than that in test reactors, it can be hypothesized that the in-service RIVE rate is overestimated by current models based on data collected from test reactors.

In the second part of this report, we explore the origins of the observed flux effect. First, Russian RIVE data of rock-forming minerals are reinterpreted using dpa analysis tailored to the specific reactor spectrum under which the irradiation experiments were conducted. Expressing the RIVE as a function of displacements per atom, rather than fast neutron fluence, offers a comparable representation of the RIVE of quartz at various irradiation temperatures. Despite this, the effects of irradiation temperature remain predominant in influencing the RIVE rate. The observed mechanisms of annealing during neutron irradiation require further studies.

As an initial step, an analysis and interpretation of post-neutron-irradiation annealing data were performed. The results indicate that thermal annealing is unlikely to be a dominant mechanism for defect healing during neutron irradiation at temperatures $\lessapprox 350$ °C.

Therefore, the apparent effect of irradiation temperature on the RIVE rate needs to interpreted differently. Higher irradiation temperatures imply greater undissipated heat due to radiation-induced energy deposition, notably from thermal neutrons and gamma rays. At this stage of the research, the hypothesis of ionization-enhanced annealing is proposed and requires further investigation.

7. REFERENCES

Bykov, V.N., A.V. Denisov, V.B. Dubrovskii, V.V. Korenevskii, G.K. Krivokoneva, and L.P. Muzalevskii. 1981. "Effect of Irradiation Temperature on the Radiation Expansion of Quartz." *Atomnaya Energiya* 51, no. 3 (September): 593–595.

Cheniour, A., Y. Li, J. Sanahuja, Y. Le Pape, E. Tajuelo Rodriguez, L. M. Anovitz, K. C. Polavaram, N. Grag, and T. M. Roseel. 2022. "FFT-based model for irradiated aggregate microstructures in concrete." *Materials and Structures* 55 (214).

Concrete Mesostructure Generation Using Python — PyCMG 1.0 documentation. Accessed June 13, 2022. https://pycmg.readthedocs.io/en/latest/.

Denisov, A.V., V.B. Dubrovskii, and V.N. Solovyov. 2012. *Radiation Resistance of Mineral and Polymer Construction Materials.* In Russian. ZAO MEI Publishing House.

Dienes, G.J., and G.H. Vineyard. 1957. *Radiation effects in solids.* Interscience Publishers.

Esselman, T., and P. Bruck. 2013. *Expected condition of concrete at age 80 of reactor operation.* Technical report A13276-R-001. 36 Main Street, Amesbury, MA 01913: Lucius Pitkins, Inc., September.

Field, K.G., I. Remec, and Y. Le Pape. 2015. "Radiation Effects on Concrete for Nuclear Power Plants – Part I: Quantification of Radiation Exposure and Radiation Effects." *Nuclear Engineering and Design* 282:126–143.

Giorla, A., and Y. Le Pape. 2015. "A Creep-Damage Model for Mesoscale Simulations of Concrete Expansion-Degradation Phenomena." In *CONCREEP 10: Mechanics and Physics of Creep, Shrinkage, and Durability of Concrete and Concrete Structures,* edited by C. Hellmich, B. Pichler, and J. Kollegger, 537–540. Vienna, Austria: American Society of Civil Engineers, September. https://doi.org/http://dx.doi.org/10.1061/9780784479346.065.

Giorla, A., Y. Le Pape, and C. Dunant. 2017. "Computing creep-damage interactions in irradiated concrete." *Journal of Nanomechanics and Micromechanics* 7 (2).

Greenwood, L.R. 1988. *Compound Displacement Damage Calculations with SPECOMP: Informal Notes.* Technical report PSR-263. Argonne National Laboratory, Radiation Safety Information Computational Center, February 28, 1988.

Greenwood, L.R., and R.K. Smither. 1985. *SPECTER: Neutron Damage Calculations for Materials Irradiations: SPECTER-ANL, PSR-263, Radiation Safety Information Computational Center.* Technical report ANL/FPP/TM-197. Argonne National Laboratory, January 31, 1985.

Hickman, B.S., and W. Pryor. 1964. "The effects of neutron irradiation on beryllium oxide." *Journal of Nuclear Materials* 14:96–110.

Hilsdorf, H.K., J. Kropp, and H.J. Koch. 1978. "The Effects of Nuclear Radiation on the Mechanical Properties of Concrete." *Special Publication of The American Concrete Institute* 55:223–254.

Hobbs, L., and M. Pascucci. 1980. "Radiolysis and defect structure in electron-irradiated α-quartz." *Journal de Physique Colloques* 41 (C6): 237–242.

Holla, Vijaya, Giao Vu, Jithender J. Timothy, Fabian Diewald, Christoph Gehlen, and Günther Meschke. 2021. "Computational generation of virtual concrete mesostructures." *Materials* 14 (14): 1–19. ISSN: 19961944. https://doi.org/10.3390/ma14143782.

Hsiao, Y.-H., E. Callagon La Plante, N.M.A. Krishnan, H.A. Dobbs, Y. Le Pape, N. Neithalath, M. Bauchy, J. Israelachvili, and G. Sant. 2018. "Role of the electrical surface potential and irradiation induced disordering on almandine's dissolution kinetics." Submitted, *The Journal of Physical Chemistry C* 122 (30): 17268–17277.

Hsiao, Y.-H., E. La Plante, N.M.A. Krishnan, Y. Le Pape, N. Neithalath, M. Bauchy, and G. Sant. 2017. "Effects of Irradiation on Albite's Chemical Durability." Submitted, *The Journal of Physical Chemistry A* 121:7835–7845.

Hsiao, Y.-H., B. Wang, E. Callagon La Plante, I. Pignatelli, N.M.A. Krishnan, Y. Le Pape, N. Neithalath, M. Bauchy, and G. Sant. 2019. "The effect of irradiation on the atomic structure and chemical durability of calcite and dolomite." Accepted, *npj Materials Degradation,* https://doi.org/10.1038/s41529-019-0098-x.

Ichikawa, T., and M. Miura. 2007. "Modified model of alkali silica reaction." *Cement and Concrete Research* 37:1291–97.

Imai, H., K. Arai, J. Isoya, H. Hosono, Y. Abe, and H. Imagawa. 1993. "centers and oxygen hole centers in synthetic silica glasses by γ irradiation." *Physical Review B* 48 (3116): 3316–3123.

Keppens, V., and C. Laermans. 1996. "Influence of heat treatment on the tunneling states in neutron-irradiated quartz." *Physical Review B* 53, no. 22 (June): 14849–61.

Krefft, G.B. 1977. "Ionization-stimulated annealing effects on displacement damage in magnisium oxide." *Journal of Vaccuum Science and Technology* 14:533–538.

Krefft, G.B., and E.P. EerNisse. 1978. "Volume expansion and annealing compaction of ion-bombarded single-crystal and polycrystalline α-Al2O3." *Journal of Applied Physics* 49, no. 5 (May): 2725–2730. ISSN: 0021-8979. https://doi.org/10.1063/1.325194. eprint: https://pubs.aip.org/aip/jap/article-pdf/49/5/2725/18379978/2725_1_online.pdf. https://doi.org/10.1063/1.325194.

Krishnan, A.N.P., Y. Le Pape, G. Sant, and M. Bauchy. 2018. "Effect of irradiation on silicate aggregates' density and stiffness." *Journal of Nuclear Materials* 512 (October 8, 2018): 126–136. https://doi.org/10.1016/j.nucmat.2018.10.009.

Krivokoneva, G.K. 1976. "Structural Changes in feldspars under Impact of Radiation." (In Russian), *Crystal Chemistry and Structural Features of Minerals* Leningrad, Nauka:75–79.

Krivokoneva, G.K., and G.A. Sidorenko. 1971. "The essence of the metamict transformation in pyrochlores." *Geochemistry International* 8:113–122.

Le Pape, Y., M.H.F. Alsaid, and A.B. Giorla. 2018. "Rock-forming minerals radiation-induced volumetric expansion – Revisiting the literature data." *Journal of Advanced Concrete Technology* 16:191–209. https://doi.org/10.3151/jact.16.191.

Le Pape, Y., K.G. Field, and I. Remec. 2015. "Radiation Effects in Concrete for Nuclear Power Plants – Part II: Perspective from Micromechanical Modeling." *Nuclear Engineering and Design* 282:144–157.

Le Pape, Y., J. Sanahuja, and M.H.F. Alsaid. 2020. "Irradiation-Induced Damage in Concrete-Forming Aggregates – Revisiting Literature Data Through Micromechanics." *Materials and Structures* 53 (62): 35. https://doi.org/10.1617/s11527-020-014.

Le Pape, Y., J.D. Tajuelo Rodriguez E.and Arregui-Mena, A. Giorla, L. Anovitz, and T.M. Rosseel. 2019. "Neutron-Irradiation-Induced Damage Assessment in Concrete Using Combined Phase Characterization and Nonlinear Fast Fourier Transform Simulation." In *Proceedings of the 10th International Conference on Fracture Mechanics,* edited by G. Pijaudier-Cabot, P. Grassl, and C. Laborderie. Bayonne, France.

Maruyama, I., O. Kontani, M. Takizawa, S. Sawada, S. Ishikawa, J. Yasukouchi, O. Sato, J. Etoh, and T. Igari. 2017. "Development of the Soundness Assessment Procedure for Concrete Members Affected by Neutron and Gamma-Irradiation." *Journal of Advanced Concrete Technology* 15:440–523.

Mayer, G, and M Lecomte. 1960. "Effet des neutrons rapides sur le quartz cristallin et la silice vitreuse." *Le Journal de Physique et le Radium* 21 (12): 846–852.

Muto, S., and I. Maruyama. 2016. *Electron irradiation-induced density change of natural rock minerals, α-quartz, orthoclase, and muscovite.* 70th Cement Technology Tournament Abstracts. 1317:120-121.

Pfeffer, R.L. 1985. "Damage center formation in SiO_2 thin films by fast electron irradiation." *Journal of Applied Physics* 57:5176–5180.

Pignatelli, I., A. Kumar, K.G. Field, B. Wang, Y. Yu, Y. Le Pape, M. Bauchy, and G. Sant. 2016. "Direct Experimental Evidence for Differing Reactivity Alterations of Minerals following Irradiation: The Case of Calcite and Quartz." Accepted for publication, *Scientific Reports – Nature* 6(20155) (January): 1–10. https://doi.org/10.1038/srep20155.

Primak, W. 1958. "Fast-Neutron-Induced Changes in Quartz and Vitreous Silica" [in English]. *Physical Review* (One Physics Ellipse, College PK, MD 20740-3844 USA) 110 (6): 1240–1254. ISSN: 0031-899X.

———. 1976. "Extrusion of quartz on ion bombardment: Further evidence for radiation-induced stress relaxation of the silica network" [in English]. *Physical Review B* (One Physics Ellipse, College Pk, MD 20740-3844 USA) 14 (10): 4679–4686. ISSN: 0163-1829.

Primak, W., and R. Kampwirth. 1968. "The radiation compaction of vitreous silica." *Journal of Applied Physics* 39 (12): 5651–5658.

Remec, I. 2013. "Radiation Environment in Concrete Biological Shields of Nuclear Power Plants." Light Water Reactor Sustainability Program.

Remec, I., T.M. Rosseel, K.G. Field, and Y. Le Pape. 2018. "Radiation-Induced Degradation of Concrete in NPPs." In *Reactor Dosimetry: 16th International Symposium,* edited by M.H. Sparks, K.R. DePriest, and D.W. Vehar, vol. ASTM STP1608, 201–211. https://doi.org/doi:10.1520/STP160820170059.

Seeberger, J., and H.K. Hilsdorf. 1982. *Einfluß von radioactiver Strahlung auf die Festogkeit and Struktur von Beton.* Technical report NR 2505. Institut für Massivbau and Baustofftechnologie, Universität Karlsruhe.

Vu, G., J.J. Timothy, D.S. Singh, L.A. Saydak, E.H. Saenger, and G. Meschke. 2021. "Numerical Simulation-Based Damage Identification in Concrete." *Modelling* 2 (3): 355–369. https://doi.org/10.3390/modelling2030019.

Walker, D.G. 1964. "Electron irradiation of beryllium oxide." *Journal of Nuclear Materials* 14:195–202. ISSN: 0022-3115. https://doi.org/https://doi.org/10.1016/0022-3115(64)90177-1.

Wang, B., Y. Yu, I. Pignatelli, G. N. Sant, and M. Bauchy. 2015. "Nature of Radiation-Induced Defects in Quartz." *The Journal of Chemical Physics* 143 (April): 024505. arXiv: 1504.02537 [cond-mat.mtrl-sci].

Whitney, D.L., and B.W. Evans. 2010. "Abbreviations for names of rock-forming minerals." *American Mineralogist* 95:185–187.

Wittels, M.C. 1957. “Structural behavior of neutron irradiated quartz.” *Philosophical Magazine* 2:1445–1461.

Wong, C.F. 1974. “Neutron radiation damage in some birefringent crystals.” *Physics Letters A* 50 (5): 346.

Yano, T., K. Fukuda, M. Imai, and H. Miyazaki. 2007. “Physical property changes of crystalline and non-crystalline SiO_2 due to neutron irradiation and recovery by subsequent annealing.” Proceedings of the Twelfth International Conference on Fusion Reactor Materials (ICFRM-12), *Journal of Nuclear Materials* 367-370:730–735.

Zinkle, S.J. 1995. “Effect of irradiation spectrum on the microstructural evolution in ceramic insulators.” Fabrication and Properties of Ceramics for Fusion Energy, *Journal of Nuclear Materials* 219:113–127. ISSN: 0022-3115. https://doi.org/https://doi.org/10.1016/0022-3115(94)00662-8.

Zubov, V.G., and A.T. Ivanov. 1966. “Expansion of quartz caused by irradiation with fast neutrons.” *Soviet Physics Crystallography* 11 (3): 372–374.

APPENDIX A. SYNTHETIC MICROSTRUCTURES

APPENDIX A. SYNTHETIC MICROSTRUCTURES

Table 12. Inclusion family data

ID	a	b	c	vf_{max}	n_{cuts}	pore	ID	a	b	c	vf_{max}	n_{cuts}	pore
1	0.15	0.15	0.15	4.38E-04	38	0	33	4.58	4.58	4.58	1.16E-03	42	0
2	0.15	0.15	0.15	3.28E-02	38	1	34	4.58	4.58	4.58	3.86E-04	42	0
3	0.3	0.3	0.3	4.38E-04	38	0	35	4.95	4.95	4.95	1.78E-02	42	1
4	0.3	0.3	0.3	3.28E-02	38	1	36	4.95	4.95	4.95	1.78E-02	42	1
5	0.45	0.45	0.45	5.14E-03	38	0	37	4.95	4.95	4.95	1.78E-02	42	1
6	0.6	0.6	0.6	7.15E-03	38	0	38	5.7	5.7	5.7	2.06E-02	43	1
7	0.6	0.6	0.6	7.88E-02	38	1	39	5.7	5.7	5.7	2.06E-02	43	1
8	0.75	0.75	0.75	6.56E-03	38	0	40	5.7	5.7	5.7	2.06E-02	43	1
9	0.9	0.9	0.9	5.20E-03	38	0	41	6.3	6.3	6.3	1.74E-02	44	1
10	1.05	1.05	1.05	3.72E-03	39	0	42	6.3	6.3	6.3	1.74E-02	44	1
11	1.2	1.2	1.2	3.21E-02	39	1	43	6.3	6.3	6.3	1.74E-02	44	1
12	1.2	1.2	1.2	3.21E-02	39	1	44	6.9	6.9	6.9	1.74E-02	44	1
13	1.2	1.2	1.2	3.21E-02	39	1	45	6.9	6.9	6.9	1.74E-02	44	1
14	1.35	1.35	1.35	1.76E-03	39	0	46	6.9	6.9	6.9	1.74E-02	44	1
15	1.35	1.35	1.35	1.76E-03	39	0	47	7.65	7.65	7.65	2.17E-02	45	1
16	1.35	1.35	1.35	1.76E-03	39	0	48	7.65	7.65	7.65	2.17E-02	45	1
17	1.65	1.65	1.65	1.09E-03	39	0	49	7.65	7.65	7.65	2.17E-02	45	1
18	1.65	1.65	1.65	1.09E-03	39	0	50	8.25	8.25	8.25	1.74E-02	46	1
19	1.65	1.65	1.65	1.09E-03	39	0	51	8.25	8.25	8.25	1.74E-02	46	1
20	1.8	1.8	1.8	2.04E-02	39	1	52	8.25	8.25	8.25	1.74E-02	46	1
21	1.8	1.8	1.8	2.04E-02	39	1	53	8.85	8.85	8.85	1.74E-02	46	1
22	1.8	1.8	1.8	2.04E-02	39	1	54	8.85	8.85	8.85	1.74E-02	46	1
23	2.55	2.55	2.55	2.41E-02	40	1	55	8.85	8.85	8.85	1.74E-02	46	1
24	2.55	2.55	2.55	2.41E-02	40	1	56	9.6	9.6	9.6	2.06E-02	47	1
25	2.55	2.55	2.55	2.41E-02	40	1	57	9.6	9.6	9.6	2.06E-02	47	1
26	2.7	2.7	2.7	1.76E-03	40	0	58	9.6	9.6	9.6	2.06E-02	47	1
27	2.7	2.7	2.7	1.76E-03	40	0	59	11.1	11.1	11.1	2.06E-02	49	1
28	2.7	2.7	2.7	1.76E-03	40	0	60	11.1	11.1	11.1	2.06E-02	49	1
29	4.05	4.05	4.05	8.37E-04	42	0	61	11.1	11.1	11.1	2.06E-02	49	1
30	4.05	4.05	4.05	8.37E-04	42	0	62	12.7	12.7	12.7	2.20E-02	50	1
31	4.05	4.05	4.05	8.37E-04	42	0	63	12.7	12.7	12.7	3.30E-02	50	1
32	4.58	4.58	4.58	7.72E-04	42	0	64	12.7	12.7	12.7	1.10E-02	50	1